Multiband Superconductivity with Unexpected Deficiency of Nodal Quasiparticles in $CeCu_2Si_2$

Sakakibara Group

The gap symmetry of unconventional superconductors has attracted much attention of scientific community because it is closely related to the exotic pairing mechanism. $CeCu_2Si_2$ (T_c ~ 0.6 K) is a historically important compound that made a breakthrough in the field of superconductivity; in 1979, exotic superconductivity was discovered for the first time in this strongly-correlated heavy-electron system [1]. Until quite recently, its gap symmetry was believed to be a nodal *d*-wave pairing mediated by spin fluctuations [2]. The presence of line nodes had been suggested from the power-law temperature dependence of various physical quantities, such as the NMR relaxation rate $1/T_1$ [3] and the specific heat, both of which were measured in the intermediate temperature region above 0.1 K. Recent interest has been focused on the location of line nodes: whether the gap symmetry is $d_{x^2-y^2}$ or d_{xy} type [4,5].

To elucidate the gap symmetry of $CeCu_2Si_2$, we performed specific-heat measurements at low temperatures down to 40 mK using a high-quality single crystal (*S*-type)[6]. Quite unexpectedly, the zero-field specific heat C_e exhibits exponential temperature dependence below 80 mK (Fig. 1(a)), reminiscent of full-gap superconductivity. In addition, we provide thermodynamic evidence for nodeless superconductivity that the low-temperature specific heat is proportional to the magnetic field at low fields for all field orientations and does not change with the *c*-plane field rotation. We found that the temperature dependence of the zero-field C_e/T including the linear behavior in the intermediate-T region can be reproduced on the basis of a phenomenological two-gap model within the conventional BCS framework using two BCS gaps, $\Delta_1 = 1.76k_BT_c$ and $\Delta_2 = 0.7k_BT_c$, whose weights are 65% and 35% of the total density of states, respectively (Fig. 1(b)). We also found anomalous behaviors in the field variations of the specific heat as well as the magnetization at low temperatures in the high-field regime (Fig. 1(c)), which can be interpreted as a strong Pauli paramagnetic effect occurring in a multiband superconductor. All the present results match with the prediction of multiband superconductivity in the absence of nodal quasiparticles.

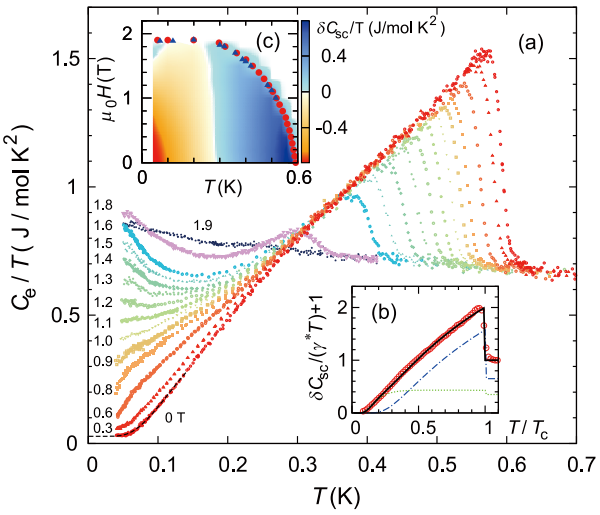

Fig. 1. (a) Temperature dependence of the electronic specific heat of $CeCu_2Si_2$ divided by temperature, C_e/T, for H // [100]. (b) Temperature dependence of C_e/T at zero field, where the T-dependent normal-state contribution is subtracted. The solid line is a best fit to the two-gap BCS model. (c) Field-temperature phase diagram for H // [100] and a contour plot of the superconducting contribution to C_e/T. Anomalous behavior that can be ascribed to the Pauli paramagnetic effect is clearly seen in the high-field and low-temperature region below 0.1 K.

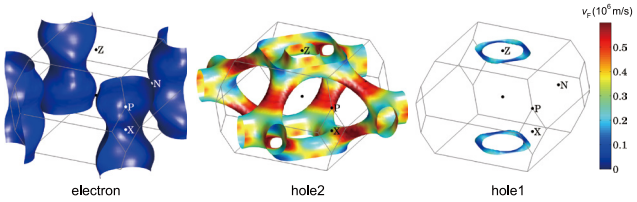

Fig. 2. The calculated Fermi surfaces of $CeCu_2Si_2$ colored by the magnitude of the Fermi velocity v_F.

One may suspect that line nodes might exist in the gap on light-mass bands, since the specific heat measurement mainly probes the heavy-mass band. To get an insight into the band structure of $CeCu_2Si_2$, we have performed first-principles calculations by the LDA+*U* method. As shown in Fig. 2, $CeCu_2Si_2$ has a flat electron band around the *X* point with the heaviest mass and two hole bands around the *Z* point. In this Fermi-surface topology, the deficiency of nodal quasiparticles requires the negligibly small effective mass of the two light-mass bands, which contradicts the multiband feature detected from the specific-heat measurement. This leads to a conclusion that the pairing symmetry of $CeCu_2Si_2$ is not the anticipated *d*-wave state, but the multiband full-gap state, including an unconventional *s*-wave such as *s*±-wave, a conventional *s*-wave, or a fully-gapped *d*+*id* state. These findings would open a new door into electron pairing in $CeCu_2Si_2$ and help understand the pairing mechanism of exotic superconductors.

References

[1] F. Steglich *et al.*, Phys. Rev. Lett. **43**, 1892 (1979).
[2] O. Stockert *et al.*, Nat. Phys. **7**, 119 (2011).
[3] Y. Kitaoka *et al.*, J. Phys. Soc. Jpn. **55**, 723 (1986).
[4] H. A. Vieyra *et al.*, Phys. Rev. Lett. **106**, 207001 (2011).
[5] I. Eremin *et al.*, Phys. Rev. Lett. **101**, 187001 (2008).
[6] S. Kittaka *et al.*, Phys. Rev. Lett. **112**, 067002 (2014).

Authors

S. Kittaka, Y. Aoki, Y. Shimura, T. Sakakibara, S. Seiro[a], C. Geibel[a], F. Steglich[a], H. Ikeda[b], K. Machida[c]

[a]Max-Planck-Institute for Chemical Physics of Solids
[b]Kyoto University
[c]Okayama University

Gapless Quantum Spin Liquid State in a Purely Organic Spin-1/2 Triangular Lattice κ-H_3(Cat-EDT-TTF)$_2$

Mori Group

A quantum spin-liquid (QSL) state is an exotic ground state where interacting spins continue to fluctuate without any formation of long-range magnetic order (LRMO) even at a sufficiently low temperature. A variety of QSL states have been theoretically predicted, but nevertheless, a systematic understanding of the elementary excitation from the experiments remains an arduous challenge. This is mainly because of the rareness of the experimental candidates, which are still restricted to the several spin-frustrated lattices, such as triangular, kagome, and hyperkagome lattices. Recently, Mori group has discovered gapless quantum spin liquid state in a purely organic spin-1/2 triangular lattice κ-H_3(Cat-EDT-TTF)$_2$ (abbreviated as κ-H)[1,2]. In this article, the results of SQUID and torque magnetometry suggesting the QSL state with gapless magnetic excitations in purely organic single-component molecular Mott insulator, κ-H, have been demonstrated [3].

Samples were prepared by the electrochemical oxidation of H_2Cat-EDT-TTF molecules in the presence of a base [1, 2]. A characteristic structural feature of this material is that, in a 2D layer, two face-to-face $(H_2Cat\text{-}EDT\text{-}TTF)^{0.5+}$ molecules form a strongly dimerized molecular unit, as shown in Fig. 1(a). Because of the strong dimerization, a dimerized unit can be treated as one site, resulting in an effective spin 1/2 per site. As schematically illustrated in Fig. 1(b), each spin is arranged on the triangular mesh with the anisotropy parameter $t'/t \sim 1.48$ at $T = 50$ K, where t and t' are the hopping integrals around the sides of rhomboids and along one diagonal, respectively. It is specific that this Mott insulator contains only conducting layers linked by hydrogen bonds without anion layers (Fig. 1(c)), namely purely organic single-component quantum spin liquid crystal.

Firstly, we measured the static magnetic susceptibility at 1 T employing a magnetic property measurement system (Quantum Design) in the temperature region from 2 to 300 K

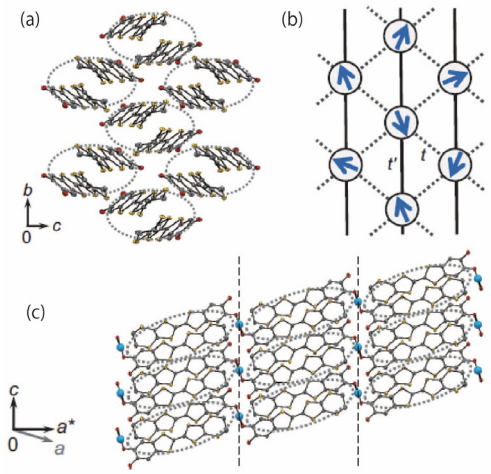

Fig. 1. (a) Molecular arrangement in a two-dimensional layer (*b*-*c* plane) of κ-H_3(Cat-EDT-TTF)$_2$. The dotted ellipsoids denote the strongly dimerized molecules. (b) A schematic of the anisotropic triangular lattice with transfer integrals *t*' and *t*. The closed circles and the arrows on them represent the sites of the triangular lattice composed of the dimerized molecules and the $S = 1/2$ spins, respectively. (c) The interlayer packing structure viewed in the *a*-*c* plane. The adjacent layers are connected by hydrogen bonds. The dotted ellipsoids represent dimerized molecules similar to those described in (a).

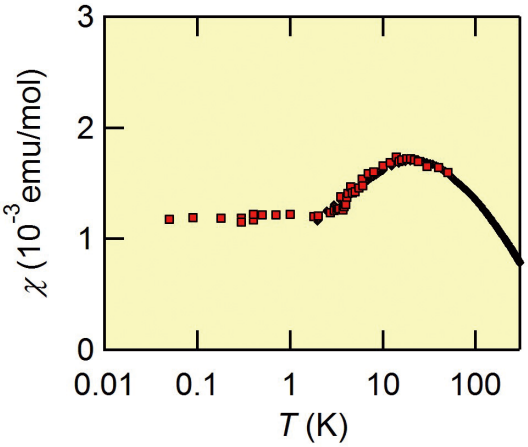

Fig. 2. Magnetic susceptibility as a function of temperature $\chi(T)$ on a semilogarithmic plot. The black diamonds denote the result of the SQUID measurement at 1 T. The red squares represent $\chi(T)$ estimated from the torque at 10 T for a–b rotation. The susceptibility $\chi(T)$ for the a–b rotation is normalized to χ(50 K) from the SQUID measurement. The $\chi(T)$ is nearly independent of temperature below $T \sim 3$ K, possibly being attributed to the Pauli paramagnetic contribution and suggesting the presence of gapless magnetic excitations in the QSL state.

using poly-crystalline samples of ~16 mg (Fig. 2). The entire temperature dependence of χ is roughly described by the $S = 1/2$ Heisenberg antiferromagnetic model of an isotropic triangular lattice, with an antiferromagnetic exchange-coupling constant $J/k_B \sim 80$–100 K. To shed light on the magnetic properties at lower temperatures, we measured the magnetic torque. As the magnetic torque only detects the anisotropic susceptibility in principle, the isotropic contribution from impurity spins is naturally eliminated, providing us with the intrinsic low temperature magnetic properties. For our system, it should be noted that sinusoidal behavior with two-fold periodicity is observed up to $H = 17$ T and down to $T = 50$ mK. Moreover, the observed amplitude of the sinusoidal torque curve is precisely proportional to the square of the magnetic field. These observations indicate that the system remains paramagnetic even at $T = 50$ mK. The above argument about the torque together with the susceptibility $\chi(T)$ reveals that spin frustration on the triangular lattice strongly suppresses the formation of long-range antiferromagnetic order even at $J/kB / T \sim 10^3$, suggesting the development of the QSL state as the ground state. Secondly, we focus on the excitation spectrum of the QSL state. In Fig. 2, $\chi(T)$ from torque magnetometory is normalized using χ determined from the SQUID measurement. What is notable in Fig. 2 is that $\chi(T)$ is nearly independent of temperature below $T \sim 3$ K, possibly being attributed to the Pauli paramagnetic contribution. This suggests the presence of gapless magnetic excitations in the QSL state.

In conclusion, we report the results of SQUID and torque magnetometry of an organic spin-1/2 triangular-lattice κ-H_3(Cat-EDT-TTF)$_2$. Despite antiferromagnetic exchange coupling at 80–100 K, we observed no sign of antiferromagnetic order down to 50 mK owing to spin frustration on the triangular lattice. In addition, we found nearly temperature-independent susceptibility below 3 K associated with Pauli paramagnetism. These observations suggest the development of gapless quantum spin liquid as the ground state. On the basis of a comparative discussion, we point out that the gapless quantum spin liquid states in organic systems share a possible mechanism, namely the formation of a band with a Fermi surface possibly attributed to spinons.

References
[1] H. Kamo, A. Ueda, T. Isono, K. Takahashi, and H. Mori, Tetrahedron Lett. **53**, 4385 (2012).
[2] T. Isono, H. Kamo, A. Ueda, K. Takahashi, A. Nakao, R. Kumai, H. Nakao, K. Kobayashi, Y. Murakami, and H. Mori, Nature Commun. **4**, 1344 (2013).
[3] T. Isono, H. Kamo, A. Ueda, K.Takahashi, M. Kimata, H. Tajima, S. Tsuchiya, T. Terashima, S. Uji, and H. Mori, Phys. Rev. Lett. **112**, 177201 (2014).

Authors
T. Isono, H. Kamo, A. Ueda, K. Takahashi[a], M. Kimata, H. Tajima, S. Tsuchiya[b], T. Terashima[b], S. Uji[b], and H. Mori
[a]Kobe University
[b]National Institute for Materials Science

Quantum Criticality in a Metallic Spin Liquid System $Pr_2Ir_2O_7$

Nakatsuji Group

At finite temperatures, electronic magnetic moments in magnetic materials are thermally fluctuating and one may have magnetic phase transitions accompanied by critical thermal fluctuations. This transition temperature can be lowered by controlling external parameters like pressure and magnetic field. In temperature near absolute zero, thermal fluctuations will be reduced, allowing quantum fluctuations to take effect. When the quantum fluctuations are strong enough, one may have a phase transition at absolute zero, namely quantum phase transition. In the vicinity of the quantum phase transition point, anomalous magnetic and metallic behaviors may be observed, such as high-T_c superconductivity in the cuprates and iron pnictides, and unconventional superconductivity in the heavy fermion systems. These phenomena are stemmed from the anomalous metallic state around the quantum critical point.

Intensive studies on quantum critical phenomena have been done on the groups of compounds so called heavy fermion systems. It is well known that the tuning of the external parameters by applying pressure or magnetic field suppresses the magnetic order down to absolute zero, leading to the emergence of quantum criticality along with the evolution of exotic phase such as anomalous superconductors. Here we have revealed the existence of quantum criticality in a metallic spin liquid system $Pr_2Ir_2O_7$, which may provide a key insight on the mechanism of large spontaneous anomalous Hall effect observed in its spin liquid state [1-4]. In this material, Pr ions form the pyrochlore structure, where the vertices of the corner sharing network of tetrahedra are occupied by Pr ions' Ising type spins, and the ferromagnetic interaction between them causes geometrically frustrated

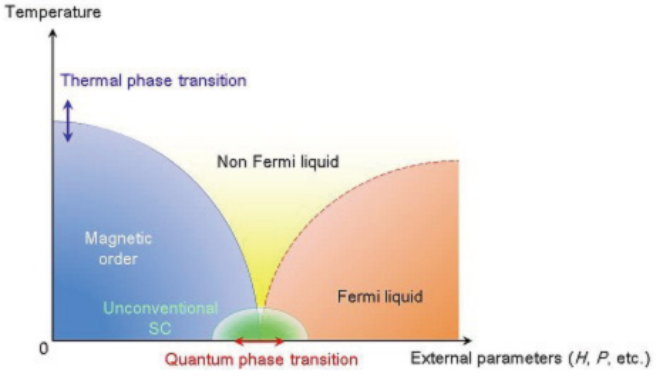

Fig. 1. Schematic phase diagram of temperature (T) vs. external parameters in strongly correlated electron systems.

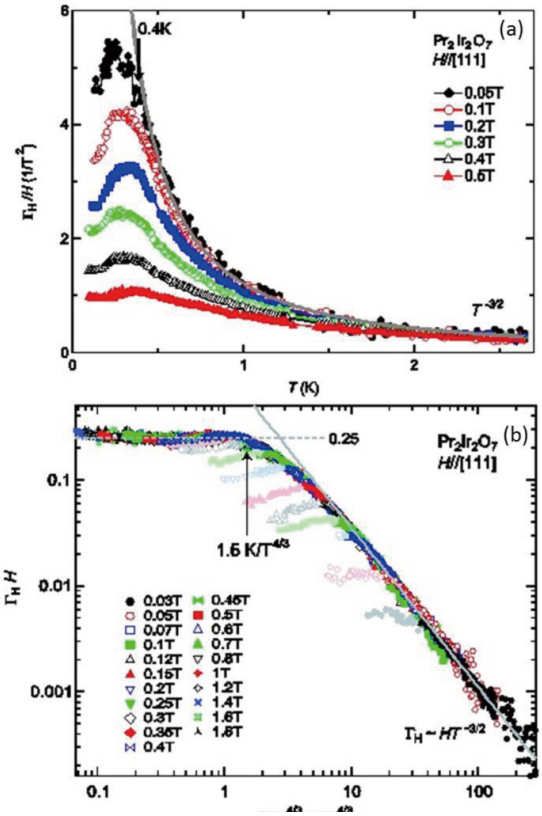

Fig. 2. (a) Temperature dependence of the magnetic Grüneisen ratio Γ_H of $Pr_2Ir_2O_7$. The divergent behavior of Γ_H appears with decreasing of a magnetic field. (b) Critical scaling of the magnetic Grüneisen ratio Γ_H for $Pr_2Ir_2O_7$. This analysis evidences a zero-field quantum critical point in the material.

spin ice state. As a result, the ground state is considered to be spin liquid, having no dipolar magnetic order. In addition, the spontaneous Hall effect appears in this spin liquid phase, suggesting the emergence of a chiral spin liquid state which has finite spin chirality.

In this study, we performed the precise magnetocaloric effect measurements on $Pr_2Ir_2O_7$ [1]. The magnetic Grüneisen ratio, which measures the change of temperature with magnetic field under adiabatic conditions, generally is known to diverge at the quantum critical point, and thus this physical quantity is very sensitive to the existence of quantum criticality.

The results show the divergence of magnetic Grüneisen ratio, indicating the existence of quantum criticality. In addition, the critical scaling which examines the position of a quantum critical point, suggests that $Pr_2Ir_2O_7$ has a quantum critical point at zero magnetic field. Therefore, this system is located at a zero-field quantum critical point without tuning of any external parameter.

In summary, we have found the zero-field quantum criticality in $Pr_2Ir_2O_7$ as indicated by the divergent Grüneisen ratio and zero-field quantum critical point. All these results suggest that the chiral spin liquid phase accompanied with the spontaneous Hall effect emerges under the influence of the quantum criticality led by geometrical frustration. This supports the manifestation of novel type of "quantum critical spin liquid" states. Our study highlights the spin ice as the parent state of the chiral spin liquid state, inducing the spontaneous Hall effects and many other intriguing quantum magnetic phenomena as represented by coherent propagation of monopoles. Our findings of quantum criticality which emerges in a spin liquid state of a highly frustrated metal

require further studies, both experimental and theoretical, on the group of frustrated metals.

References
[1] S. Nakatsuji *et al*., Phys. Rev. Lett. **96**, 087204 (2006).
[2] Y. Machida, S. Nakatsuji, Y. Maeno, T. Tayama, T. Sakakibara, and S. Onoda, Phys. Rev. Lett. **98**, 057203 (2007).
[3] L. Balicas, S. Nakatsuji, Y. Machida, and S. Onoda, Phys. Rev. Lett. **106**, 217204 (2011).
[4] Y. Machida, S. Nakatsuji, S. Onoda, T. Tayama and T. Sakakibara, Nature **463**, 210 (2010).
[5] Y. Tokiwa, J. J. Ishikawa, S. Nakatsuji, and P. Gegenwart, Nat. Mater. **13**, 356 (2014).

Authors
Y. Tokiwa[a], J. J. Ishikawa, S. Nakatsuji, and P. Gegenwart[a]
[a]University of Augsburg

Superconductivity in Anti-Post-Perovskite Vanadium Compound

Ohgushi Group

Superconductivity, which is a quantum state induced by spontaneous gauge symmetry breaking, frequently emerges in quasi-two-dimensional materials. The typical examples are high-critical-temperature cuprate with the layered-perovskite (pv) structure, and other examples include a ruthenate Sr_2RuO_4, boride MgB_2, hafnium nitride chloride, cobaltate $Na_xCoO_2{\bullet}yH_2O$, an intercalated graphite C_6Ca, and iron-based pnictides and chalcogenides. Hence, the layered character of the host crystal structures is widely believed to be essential in producing superconductivity. This provides an important hint for exploring new superconducting materials. Recently, the post-perovskite (ppv) structural transition of $MgSiO_3$ was discovered under extremely high-pressure (~120 GPa), and captures great interests because the ppv $MgSiO_3$ is considered to be the main constitute of the Earth's lowermost mantle, D" layer [1]. The ppv structure has a peculiar two-dimensional character, and is expected to be a good platform for superconductivity. However, up to now, no superconductivity has been observed in isostructural materials.

We here report the discovery of superconductivity in the anti-post-perovskite (anti-ppv) compounds [2]. We focused on the vanadium compound V_3PN with an anti-ppv structure, where the anion and cation positions are reversed with respect to the ppv structure. We then demonstrated that the compound exhibits superconductivity below 4.2 K (Fig. 1). This is the first report of superconductivity in an isostructural compound. Even though the critical temperature is limited to low temperatures at present, it should be possible to increase the critical temperature by optimizing chemical composition. Indeed, the critical temperature reaches the maximum value of 5.6 K in a slightly N-deficient compound, V_3PN_x with x = 0.9. This discovery stimulates further explorations of new superconducting materials with ppv and anti-ppv structures.

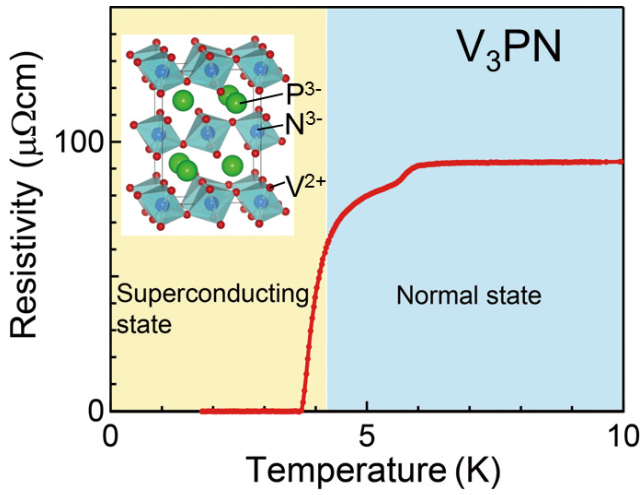

Fig. 1. The resistivity of an anti-post-perovskite compound V_3PN. The resistivity drops to zero at low temperature, indicating the onset of superconductivity. The inset shows the crystal structure.

References
[1] M. Murakami, K. Hirose, K. Kawamura, N. Sata, and Y. Ohishi, Science **304**, 855 (2004).
[2] B. Wang and K. Ohgushi, Scientific Reports **3**, 3381 (2013).

Authors
B. Wang and K. Ohgushi

Quantum Phase Transitions of the Hubbard Model on the 1/5-Depleted Square Lattice

Ueda Group

Quantum phase transition is one of the central issues of the present-day condensed matter physics. One of the routes to approach quantum criticality is to introduce geometrical frustration. Another way is to deplete lattice sites periodically, leading to weaker connectivity. A typical example is depletion from the triangular lattice: One can obtain the honeycomb lattice by the 1/3-depletion and the kagome lattice by the 1/4-depletion. It is interesting to note that the tight-binding models on the depleted lattices often show peculiar dispersions like flat bands and/or Dirac cones.

In the present study [1, 2, 3] we investigate Hubbard model on the 1/5-depleted square lattice, Fig. 1. Although the lattice structure looks very artificial, this structure can be found in nature in CaV_4O_9 or $K_{0.8}Fe_{1.6}Se_2$. The unit cell of this lattice contains four sites and thus the energy band structure of the non-interacting system has four bands. At the symmetric point where $t_1 = t_2$ the lowest band and the third one touch at the Γ point, forming a Dirac cone. The second lowest band intersects the apex of the Dirac cone. Therefore this characteristic dispersion is relevant to quantum phase transitions of the Hubbard model on this lattice at quarter filling [1, 2]. With the Coulomb interaction the ground state phase diagram obtained by the mean field theory changes from the non-magneteic insulating phase to the paramagnetic metallic phase, then to an antiferromagnetic metallic phase, and finally to an antiferromagnetic insulating phase, as the ratio t_2/t_1 is increased. Since the Dirac cone is embedded in threefold degenerate electronic states the effective theory around the Γ point is SU(3) Dirac electrons. The rich phase diagram of the Hubbard model is understood by using this effective theory.

The quantum phase transitions at half-filling are also very interesting [3]. It has been known that the Heisenberg model, which is the effective Hamiltonian in the strong correlation limit, shows two quantum phase transitions, one from the dimer singlet phase to the insulating phase with the antiferromagnetic long range order and then onto the plaquette singlet phase. We have looked at the quantum phase transitions of the Hubbard model as a function of Coulomb interaction

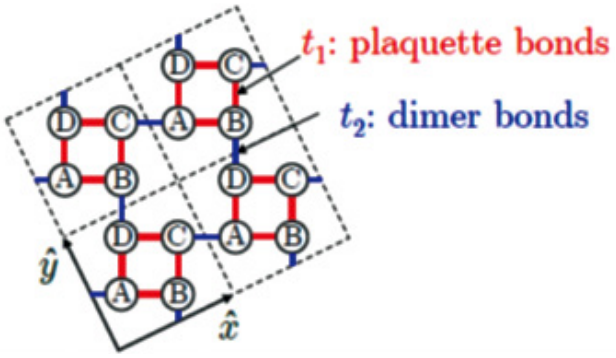

Fig. 1. The 1/5-depleted square lattice. One can define either the unique plaquette covering or the dimer covering. We consider the Hubbard model on this lattice with different hopping matrix elements for the plaquette bonds or the dimer bonds.

under the assumption of paramagnetic states. The nature of the metal-insulator transition is different depending on the ratio of t_2/t_1. On the dimer side, it is shown by applying the cluster dynamical mean field theory that the metal-insulator transition is continuous. This continuous Mott transition is characterized as a Lifshitz transition driven by the Coulomb interaction.

References
[1] Y. Yamashita, M. Tomura, Y. Yanagi, and K. Ueda, Phys. Rev. B **88** 195104 (2013).
[2] Y. Yamashita, M. Tomura, Y. Yanagi, and K. Ueda, JPS Proceedings, SCES2013.
[3] Y. Yanagi and K. Ueda, JPS Proceedings, SCES2013.

Authors
Y. Yamashita[a], M. Tomura, Y. Yanagi[b], and K. Ueda
[a]Nihon University
[b]Tokyo University of Science

Structural Evolution of 1D Spectral Function from Low- to High-Energy Limits

Takada Group

The concept of spin-charge separation plays a central role in describing low-energy physics near Fermi points in a one-dimensional (1D) interacting electron gas, a typical example of the spin-1/2 Luttinger liquid (LL). This concept may be confirmed in real materials by various experiments, including the recent high-resolution angular resolved photoemission spectroscopy in which the one-electron spectral function $A(p,\omega)$ can be directly measured in the wide range of momentum p and energy ω.

If p is not restricted to the region near the Fermi momentum p_F, the linear spectrum approximation, usually adopted in the LL theory, is not sufficient in appropriately obtaining $A(p,\omega)$. In fact, the effect of the nonlinear spectrum on $A(p,\omega)$ has been intensively studied in recent years. According to those studies on integrable systems, $A(p,\omega)$ has singularities for arbitrary p in proportion to $|\omega-\varepsilon_\nu(p)|^{-\mu_\nu(p)}$ with ν=s and c, where $\varepsilon_s(p)$ and $\varepsilon_c(p)$ are energies of spin and charge collective excitations, respectively. In the usual LL theory, the exponent $\mu_\nu(p)$ is independent of p, but the nonlinearity in the electron dispersion makes it depend on p. Since the edge of support of $A(p,\omega)$ is located at $\omega=\varepsilon_s(p)$, $\mu_s(p)$ determines the power of the threshold singularity in $A(p,\omega)$ and its actual value has been given from the finite-size spectrum obtained by the Bethe-ansatz method. For nonintegrable systems, this threshold singularity remains intact, but the singularity at $\omega=\varepsilon_c(p)$ is smeared into a broad peak.

In those preceding works, only the singularities at $\omega=\varepsilon_s(p)$ and $\omega=\varepsilon_c(p)$ are discussed on the belief that the electron nature will not sustain in the spin-charge separated system. For p far away from p_F, however, the effect of interactions becomes so weak that we would naively expect that the nature of an injected electron to measure $A(p,\omega)$ manifests itself as a main peak in $A(p,\omega)$. Then a natural question arises: ***Does an electron-like excitation mode actually exist in the 1D interacting electron gas for p much larger than p_F?*** If yes, a related and more intriguing question is: ***How does the electron-like mode reconcile with the physics of spin-charge separation for p near p_F?***

In pursuit of answers to those questions, we have carefully studied the 1D one-electron Green's function $G(p,t)$ in momentum space and time and found that for $p\sim p_F$, its long-time asymptotic form is composed of ***three*** independent modes of power-law decay [1]. Two of them correspond to well-known spinon and (anti)holon excitations, but the rest describes the mode of an electron-like particle (***pseudoelectron***) which may be regarded as an electron dressed with a "cloud" of low-lying spin and charge collective excitations. This pseudoelectron does not appear as a main structure in $A(p,\omega)$ for $p\sim p_F$ and never leads to a finite jump in the momentum distribution function $n(p)$. As p goes away from p_F, the pseudoelectron structure gets broader, but with the further increase of p, it becomes less broad and eventually for $p>>p_F$, it evolves as a main and divergent peak in $A(p,\omega)$ by swallowing the antiholon mode. Concomitantly, its dispersion relation approaches the one of a free electron, allowing us to regard the pseudoelectron as a free electron, but actually it is not quite, nor the Landau's quasiparticle, basically because this excitation is accompanied by power-law decay. Those results clarify the generic feature of $A(p,\omega)$ in a 1D metal and answer the aforementioned two questions.

As an illustration of the overall behavior of $A(p>p_F,\omega)$ with the change of p and ω, we adopt the Yang-Gaudin model in the weak-coupling region in order to explicitly compute $A(p,\omega)$. In Fig. 1, the obtained result is displayed with increasing p from p_F to show its complete structural evolution in the 1D weakly-interacting electron gas with the quadratic dispersion ξ_p ($=p^2/2m-p_F^2/2m$). Since we focus on the region of ω in the very vicinity of ξ_p, only the pseudoelectron mode appears as a singular structure in $A(p,\omega)$ in Fig. 1.

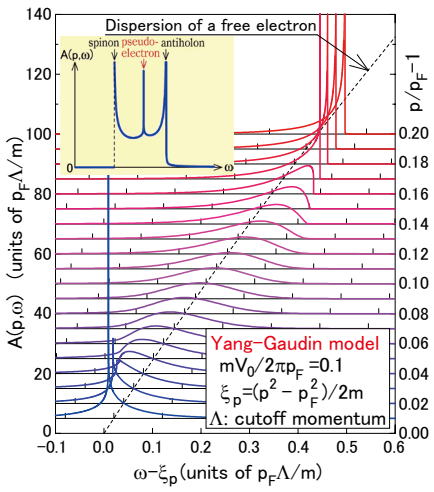

Fig. 1. Structural change of the pseudoelectron peak in the one-electron spectral function $A(p,\omega)$ for the Luttinger liquid (Yang-Gaudin model). Inset: The entire structure of the spectral function near the Fermi point.

The pseudoelectron introduced here very much resembles a quasiparticle in higher-dimensional Fermi-liquid systems, although it is not quite the same, reflecting the specialty of 1D physics. We hope that this concept of a pesudoelectron will be confirmed in the future through experiment and/or large-scale numerical calculation with deliberately-chosen parameters so as to avoid its overdamping regime.

Reference
[1] H. Maebashi and Y. Takada, Phys. Rev. B 89, 201109 (R) (2014).

Authors
H. Maebashi and Y. Takada

Particle Statistics, Frustration, and Ground-State Energy

Oshikawa Group

Quantum statistics of identical particles is one of the most fascinating aspects of quantum mechanics. The wavefunction does not change when two identical bosons are exchanged, while it acquires a negative sign when two identical fermions are exchanged. This fundamental distinction leads to various differences in physical properties between a system of many bosons and that of many fermions. For example, fermions obey Pauli exclusion principle, which forbids more than one particles to occupy the same single-particle state. In contrast, any number of bosons can occupy the same single-particle state, concerning the quantum statistics. In fact, at sufficiently low temperatures, a macroscopic number of bosons may occupy the same single-particle state. This is the celebrated Bose-Einstein Condensation, which has been directly observed in ultracold atoms.

Let us consider two systems with the "identical" Hamiltonian, but the one consists of many bosons and the other consists of many fermions. By "identical" Hamiltonian we mean the single-particle eigenstates and their energy eigenvalues are identical. Our question is: which system has the lower ground-state energy, the one of bosons or that of fermions? It might appear a trivial question, since in the ground state all the bosons will occupy the lowest-energy single-particle eigenstate, while most of the fermions will occupy higher energy single-particle eigenstates because of the Pauli exclusion principle. Then the ground-state energy of fermions would be always higher than that of bosons. However, this simple argument is only valid when there is no interaction. When there is an interaction between the particles, as is the case in realistic systems, the Bose-Einstein Condensation is not perfect. Thus the comparison is a nontrivial question in the presence of interaction.

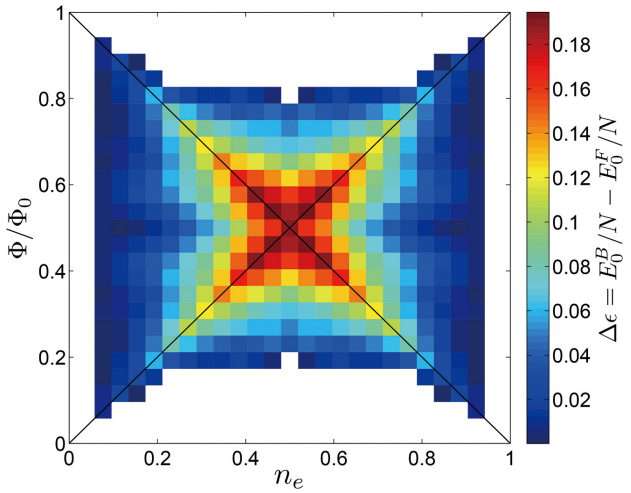

Fig. 1. Comparison of the ground-state energies of fermions and hard-core bosons on the square lattice of 26 sites. The horizontal axis is the number of particles ne per site, and the vertical axis is the flux per plaquette Φ in unit of the flux quantum Φ_0. The ground-state energy of fermions is lower than that of bosons in the colored region, and the difference is most significant in the red-colored region, where $n_e = \Phi/\Phi_0$ or an equivalent relation approximately holds.

We first proved [1] a theorem which states: even in the presence of interaction, bosons have a lower ground-state energy if all the hopping amplitudes are positive. This theorem can be understood in terms of frustration among quantal phases; if all the hopping amplitudes are positive, there is no such frustration in the system of bosons while fermions are subject to frustration due to their quantum statistics. We can violate the assumption of the theorem by introducing negative and/or complex hopping amplitudes. This makes it possible that the inequality between the ground-state energies to be reversed. This again can be understood in terms of frustration introduced among hoppings. In fact, we succeeded in constructing several concrete examples, in which the ground-state energy of fermions is lower than that of corresponding bosons [1]. This includes a rigorous proof on the delta-chain case, for which the reversal was reported earlier on small clusters [2].

References
[1] W. Nie, H. Katsura, and M. Oshikawa, Phys. Rev. Lett. **111**, 100402 (2013).
[2] S. D. Huber and E. Altman, Phys. Rev. B **82**, 184502 (2010).

Authors
W. Nie, H. Katsura[a], and M. Oshikawa
[a]Gakushuin University

K-computer Simulation for Electrochemical Energy Conversion

Sugino Group

Energy flows through matters in various forms and controlling the energy flow is an important subject of interdisciplinary material research. The energy flow dynamics is complex but is particularly rich near the interface, where the energy carrier (particle or field) switches from one to another. The electrochemical interface offers a field for converting an *ionic flow* to the *electronic flow*, and this conversion process is used as the principle of a battery. The corresponding basic process is the electron-transfer reaction dynamics, which has now attracted renewed attention not only from electrochemistry but also from many other fields. In this context, this group is intended to describe the dynamics, with the help of the K-computer power, unambiguously within the first-principles molecular dynamics (FPMD) scheme. A simulation team was organized from research groups of Osaka/Tohoku/Nagoya University and national laboratories (AIST and NIMS). The joint simulation team has recently made progress toward the goal.

The team modeled the system using a metal slab, a solution slab, and the dielectric continuum slab as shown in Fig. 1. This model, called the effective screening medium (ESM) model, was originally developed by the present group in 2006 [1] but was recently improved to enable a precise

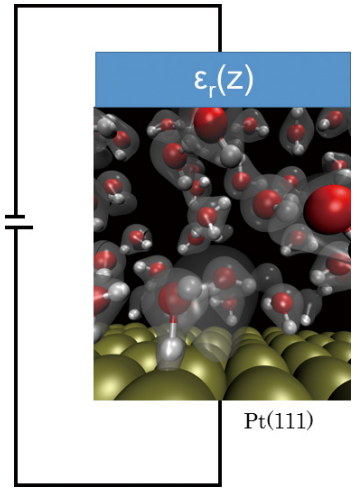

Fig. 1. The ESM modeling of the electrochemical interface. The model consists of the electrode slab (Pt(111) in the present case), solution slab (liquid water plus a hydronium ion) and the dielectric continuum. The continuum is characterized by the dielectric constant. The bias potential is controlled with the potentiostat scheme [2].

control of the bias potential [2,3]. By this technique one can describe a subtle imbalance of chemical equilibrium between the electrons and the ions, essential for studying an electrochemical process. This algorithm was implemented to an FPMD code, called STATE-senri, which had been highly parallelized for K-computer.

One of the first target of this new FPMD scheme was to investigate how the solvent fluctuation would affect the catalytic activity. The solvent fluctuation causes the bias potential to fluctuate, whereby assisting the catalytic reaction to occur. The fluctuation is small for the bulk catalysts but is increasingly enhanced as the catalyst is reduced in size. By combining the simulation with the classical Marcus theory, the exchange current for the reaction, which is a measure of catalytic activity, was found to be enhance by 15 when the size of nano-particle is reduced to 3 nm in diameter [4]. This enhancement factor is indeed a large value which is comparable to (or larger than) that achievable with the nano-shell method, i.e., a technique to enhance the activity by alloying the subsurface Pt. The fluctuation effect has not been seriously studied so far, but the present calculation suggests further room for enhancing the catalytic activity by controlling the structure of the interface.

This group has been performing a large number of first-principles simulations, with or without the ESM, and the results have accumulated. With those data, this group has reconsidered how the reduction of an oxygen molecule would occur, which is the central issue of electrochemistry and many efforts have been devoted. When the simulation results were analyzed together with recently available experimental results, it was found that some of the reaction pathways can be excluded and accordingly narrowed down the possibilities [5]. It was then concluded that the reaction proceeds mainly through a pathway called the associative pathway in the steady state, while the other one, called the dissociative pathway, is chosen prior to steady state. This analysis emphasizes importance of the dynamical effect in discussing the dominant mechanism.

More extensive simulations are now conducted in K-computer. The team is preparing further for the coming exa-flops supercomputers to establish a microscopic theory of electrochemical energy conversion.

References
[1] M. Otani and O. Sugino, Phys. Rev. B **73**, 115407 (2006).
[2] N. Bonnet, T. Morishita, O. Sugino, and M. Otani, Phys. Rev. Lett. **109**, 266101 (2012).
[3] I. Hamada, O. Sugino, N. Bonnet, and M. Otani, Phys. Rev. B **88**, 155427 (2013).
[4] N. Bonnet, O. Sugino, and M. Otani, J. Chem. Phys. **140**, 044703 (2014).
[5] N. Bonnet, O. Sugino, and M. Otani, to be published in J. Phys. Chem. C.

Authors
O. Sugino,[b] N. Bonnet,[b] I. Hamada[a], M. Otani[a], T. Ikeshoji[a], Y. Morikawa[b], K. Inagaki[b], H. Kizaki[b], K. Akagi[c], M. Araidai[d]
[a]Advanced Industrial Science and Technology
[b]Osaka University
[c]Tohoku University
[d]Nagoya University

Kondo Signature in Heat Transfer via a Local Two-State System

Kato Group

Heat and electric transport have several similarities as well as dissimilarities. Fourier's law in heat transport corresponds to Ohm's law in electric transport, and these laws are commonly categorized as diffusive transport. Ballistic transport leads to the quantization of conductance in electric as well as heat transport. The conductance quantum was measured in mesoscopic electric conduction in 1988, and much later, the version of heat transport was also measured [1]. Recently, the concept of thermal diode has also been discussed, and an experiment has been conducted for demonstrating this [2]. Recent progress in transport studies strongly indicates that heat transport analogue exists for many categories of electric transport.

We have studied the Kondo effect in heat transport via a local two-state system [3]. We consider a two-state system coupled to phonon environments. The two-state system is, for example, obtained from truncation from a symmetric double-well system with a small tunneling matrix element Δ. The present system is described by the spin-boson Hamiltonian with Ohmic dissipation. The cut-off energy of the phonon bath and the dimensionless system-environment coupling are denoted with ω_c and α, respectively. It is known that the spin-boson model can be mapped onto the Kondo model with anisotropic exchange coupling. In order to

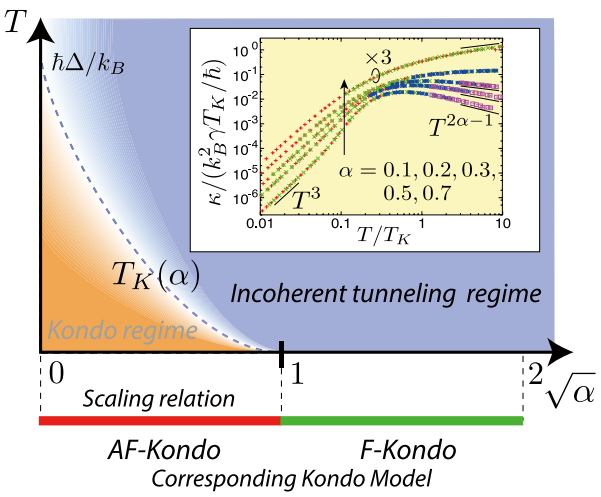

Fig. 1. (Main panel) Two different regimes expected in the spin-boson model. (Inset) The thermal conductance calculated by the quantum Monte Carlo method is shown as a function of the temperature.

study the Kondo-like effect in the phonon systems, we have derived the exact formula of thermal conductance, and have evaluated it by the quantum Monte Carlo method.

Summary of the results is shown in Fig. 1. The main figure shows the Kondo regime and the incoherent tunneling regime in the space of temperature T versus dimensionless coupling strength α. At the bottom of the main figure, mapping onto corresponding anisotropic Kondo model is shown: the antiferromagnetic Kondo (AF-Kondo) and the ferromagnetic Kondo (F-Kondo) region are respectively mapped onto the region of $0<\alpha<1$ and $1<\alpha<4$ in the spin-boson Hamiltonian. Heat transport via the Kondo effect is realized in the Kondo regime (the orange region).

In the inset of the figure, we show temperature dependence of the thermal conductance κ calculated by the quantum Monte Carlo method. Different legends in the graph denote with different ratios of Δ/ω_c. As seen in the figure, the data for a fixed α fall onto one curve by appropriate scaling of the temperature and the thermal conductance with the Kondo temperature T_K. This behavior is characteristic of the Kondo effect. Below the Kondo temperature, conductance follows the universal temperature dependence proportional to T^3. The obtained thermal conductance is much larger than the one expected from stochastic transition of the two-state system [4]. This is a manifestation of strong correlation between system and reservoirs, which is analogous to the Kondo effect in electric transport. On the other hand, at temperatures higher than the Kondo temperature T_K, the thermal conductance becomes proportional to $T^{2\alpha-1}$. This behavior is understood by a simple approximation based on the Fermi's golden rule. We note that the thermal conductance is always proportional to $T^{2\alpha-1}$ for $\alpha>1$ since the Kondo temperature is zero.

In summary, we have investigated the Kondo effect in thermal transport via a local two-state system, by utilizing the spin-boson model with ohmic dissipation. We hope that our study motivates further research on low-energy heat transfer via local systems. Other types of dissipation (superohmic/subohmic dissipation) and far-from-equilibrium effect will be intriguing subjects in this direction.

References

[1] B. J. Wees *et al.*, Phys. Rev. Lett. **60**, 848 (1988); K. Schwab *et al.*, Nature (London) **404**, 974 (2000); H.-Y. Chiu *et al.*, Phys. Rev. Lett. **95**, 226101 (2005).
[2] N. Li, J. Ren, L. Wang, G. Zhang, P. Hänggi, and B. Li, Rev. Mod. Phys. **84**, 1045 (2012); C. W. Chang, D. Okawa, A. Majumdar, and A. Zettl, Science **314**, 1121 (2006).
[3] K. Saito and T. Kato, Phys. Rev. Lett. **111**, 214301 (2013).
[4] T. Ruokola and T. Ojanen, Phys. Rev. B **83**, 045417 (2011).

Authors
K. Saito[a] and T. Kato
[a]Keio University

Nature of Spin Polarization in a Quantum Point Contact

Katsumoto Group

Creation of spin current in quantum structures of non-magnetic materials is a key technique in semiconductor spin-electronics (spintronics). The use of spin-orbit interaction (SOI) and quantum point contact (QPC) structure is a promising candidate. So called Rashba-type SOI

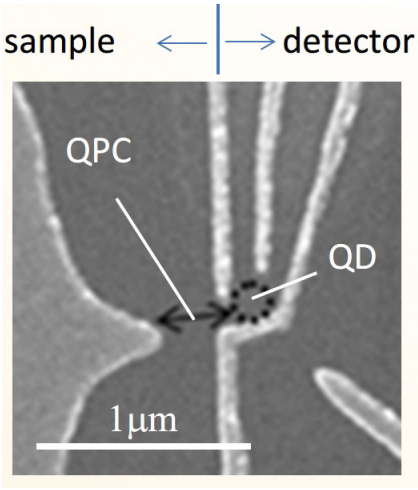

Fig. 1. Scanning electron micrograph of the gate configuration for the sample. The gray regions are metallic Schottky gates.

splits electronic spin states according to the direction of momentum. Electronic states in a QPC structure are a set of one-dimensional bands with discrete edges due to quantization transverse to the one-dimensional motion. As a result, ordinary conductance of a QPC is quantized with the unit of $2e^2/h$, which is called conductance quantum. There are a number of experimental reports on the anomalous quantization of conductance at a half conductance quantum, i.e. e^2/h, which phenomenon, called 0.5 conductance plateau has been attributed to the result of perfect spin polarization [1] though direct evidence was not obtained. Such a high spin polarization was also predicted on the 1.0 plateau (i.e. $2e^2/h$) [2] but due to the lack of detection method, there have been no experimental confirmation.

We have developed a new technique for the detection of spin-polarization with time-domain spin blockade. For that the two-electron tunneling process from the target device to a quantum dot (QD) is used. When the process is to a single orbital level, the probability is suppressed while it is not for the tunneling into two orbital levels. Hence the degree of suppression has a direct relationship to the spin-polarization in the target with the spin-relaxation time in the QD as a parameter.

As the base system, two-dimensional electron gas (2DEG) in an (In, Ga)As quantum well was adopted. The sample consists of a QPC with a side-coupled QD with another QPC for the remote charge detection (Fig. 1). The conductance of the QPC as a function of the gate voltage shown in Fig. 2 clearly exhibits 0.5 anomalous plateau struc-

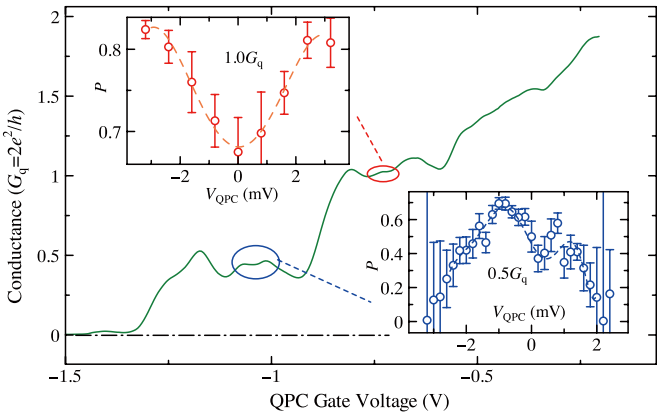

Fig. 2. QPC conductance as a function of the gate voltage. The unit is the quantum conductance $G_q=2e^2/h$. The insets show bias voltage (V_{QPC}) dependence of spin-polarization of 0.5 G_q and 1.0 G_q plateaus respectively.

ture in addition to the ordinary quantized plateau at $2e^2/h$. Spin-polarization measured with the QD detector is shown as a function of the QPC bias voltage V_{QPC} in the insets of Fig. 2, both for 0.5 and 1.0 plateaus. Here the definition of spin-polarization P is $P = (N_u–N_d) / (N_u+N_d)$, where N_u and N_d correspond to the concentration of up-spin electrons and down-spin electrons respectively. At zero-bias voltage, P is high on 0.5 plateau while it decreases with increasing V_{QPC}. The differential conductance of the QPC, on the contrary, increases with V_{QPC} indicating that the mechanism of the spin-polarization is a kind of spin-filtering, which cuts the flow of spin-down electrons. On the other hand at 1.0 plateau, P gradually increases with V_{QPC}, indicating that the mechanism here is spin-rotation, which turns up the down spin of electrons. There is a small dip structure in P near the zero-bias at 0.5 plateau, which reflects the formation of the Kondo cloud. As just described we have demonstrated the powerfulness of the present method and revealed the mechanisms of spin-polarization in a QPC with Rashba-type SOI.

References

[1] P. Debray *et al.*, Nature Nanotechnology **4**, 759 (2009).
[2] M. Eto, T. Hayashi, and Y. Kurotani, J. Phys. Soc. Jpn. **74**, 1934 (2005).
[3] M. Kohda *et al.*, Nature Communications **3**, 1082 (2012).

Authors

S. Katsumoto, S.W. Kim, T. Nakamura, and Y. Hashimoto

Spin Injection into a Superconducting Niobium

Otani Group

Spintronics is a spin counterpart of electronics and its potentiality for future applications as well as for novel physics has boosted a number of researches in recent years. Among diverse materials, superconductors are promising for their distinct properties of spin transport; because of a superconducting energy gap, spins are mediated by quasiparticles and it is theoretically predicted that the spin relaxation time (τ_s) is enhanced owing to the reduced group velocity of quasiparticles. However, previous experimental studies are not conclusive due to the problems of device structures. Thus, for both basic physics and applications, it is highly desirable to estimate τ_s in superconductors *correctly* without spurious effects. In this work [1], we aimed at injecting a pure spin current into superconductors with a large spin-orbit (SO) interaction and estimating τ_s appropriately. Through the use of such superconductors, we can expect more complex phenomena for further studies where superconductivity, magnetism and SO interaction are closely coupled.

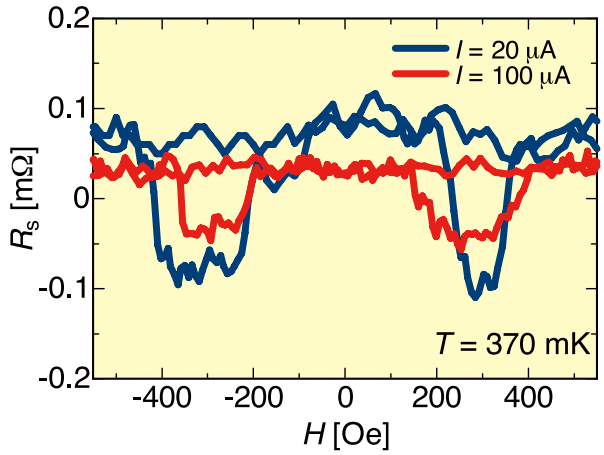

Fig. 1. NLSV signals R_s measured at 370 mK (< T_C) with two different currents I = 20 μA (red) and 100 μA (blue).

We fabricated a typical lateral spin valve structure with a superconductor Nb, consisting of two ferromagnetic Permalloy ($Ni_{81}Fe_{19}$; Py) wires bridged by a nonmagnetic Cu wire and a Nb wire inserted below the Cu bridge in between the two Py wires. By flowing a charge current (I) from one of the Py wires to the Cu, a pure spin current is generated in the Cu bridge and partly absorbed into the Nb due to its large SO interaction. The pure spin current can be detected by the other Py wire, and the detected nonlocal spin valve (NLSV) signal is reduced when the spin absorption occurs. In our study we performed spin absorption measurements both above and below the critical temperature of Nb (T_C = 5.5 K).

In Fig. 1, we show a result of the spin absorption measurements taken at 370 mK, much lower than T_C. The NLSV signal shown here is normalized by I. Above T_C, it is independent of I (not shown here), as expected for normal metals. Far below T_C, on the other hand, the NLSV signal obviously increases as I decreases, indicating the suppression of the spin absorption at the Nb wire. In order to evaluate the amount of the pure spin current absorbed from Cu into Nb, we calculated the density of states of the superconducting Nb using the Usadel equation where the superconducting proximity effect between Cu and Nb is taken into account. In the Usadel equation, τ_s of the superconducting Nb is treated as a free parameter. With this parameter, we can reproduce the NLSV signal for each I, and simultaneously obtain τ_s. The obtained data are shown in Fig. 2. τ_s is clearly enhanced with decreasing I. To know the relation between I and temperature, we also measured the interface resistance between Cu and Nb as functions of I and temperature, and found that the effective temperature (T) at the interface is increased by I. These results clearly demonstrate the enhancement of τ_s in a superconductor with decreasing T consistent with the theoretical prediction [2].

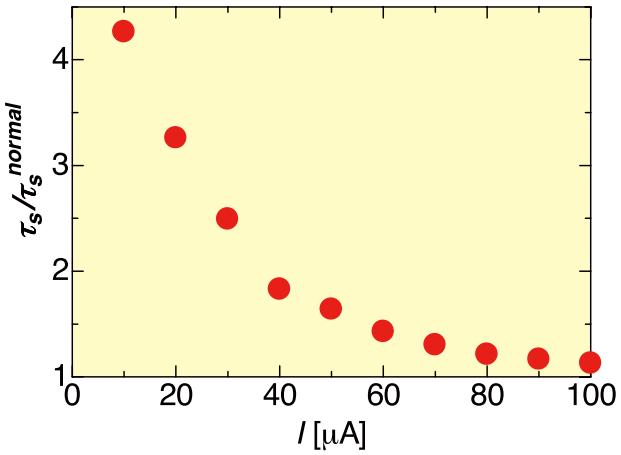

Fig. 2. The relation between τ_s and I. τ_s is normalized by that in the normal state (τ_s^{normal} = 2.3 × 10^{-13} s). As I decreases, τ_s dramatically increases.

References

[1] T. Wakamura, N. Hasegawa, K. Ohnishi, Y. Niimi, and Y. Otani, Phys. Rev. Lett. **112**, 036602 (2014).
[2] T. Yamashita, S. Takahashi, H. Imamura, and S. Maekawa, Phys. Rev. B **65**, 172509 (2002).

Authors

T. Wakamura, N. Hasegawa, Y. Niimi, and Y. Otani

One-dimensional Fermi Surface is Stabilized on Ge Surface Even at Low Temperature

Komori group

In solid-state physics, we learn that electrons in one-dimensional metals undergo metal-to-insulator transition induced by the Peierls instability due to electron-phonon interaction or exhibit a Luttinger liquid behavior due to electron-electron interaction with decreasing temperature. Atomic nanowires formed on semiconductor surfaces offer an opportunity to investigate such intriguing phenomena of one-dimensional metals. So far, however, their manifestations are largely disturbed by the presence of defects in the nanowires. Highly-ordered atomic nanowires at surfaces are thus essential not only for clarifying if they exhibit the Peierls instability or a Luttinger liquid behavior, but also for understanding universal nature of one-dimensional electronic systems. On the Ge(001) surface, defect- and kink-free Pt-induced atomic nanowires (Pt/Ge(001) NWs) can be formed, and are very suitable for the study of one-dimensional electrons. [1,2,3] We have investigated the ground-state electronic properties of Pt/Ge(001) NWs at the Fermi level (E_F) *in situ* by angle-resolved photoelectron spectroscopy at 6 K, a sufficiently lower temperature than its structural phase transition at 80 K, using single-domain samples shown in Fig. 1.

Figure 2(a) shows the Fermi-surface mapping at 6 K. Two metallic surface bands labeled S_1 and S_2 are clearly identified. The Fermi surface of S_1 consists of straight lines in the k_y direction, indicating that the S_1 band disperses only in the nanowire direction. It is therefore an ideal one-dimensional metallic state which is decoupled from neighboring electronic systems. As shown in Fig. 2(b,c), it exhibits a steep dispersion and clearly crosses E_F in the substrate bulk band gap. Obviously, there is no gap opening at E_F. Thus, the S_1 band does not directly contribute to the structural phase transition at 80 K and is stable against the Peierls instability if it exists. The electron-phonon interaction could not be strong enough to induce any structural transition with the nesting vector for S_1 by the Peierls instability scheme. In order to examine a Luttinger liquid behavior, the energy distribution curve of S_1 was analyzed as shown in Fig. 2(d). The observed spectral shape agrees with the normal Fermi-Dirac-type distribution function without any indication of the power-law behavior predicted for a Luttinger liquid. These novel results provide not only a valuable contribution

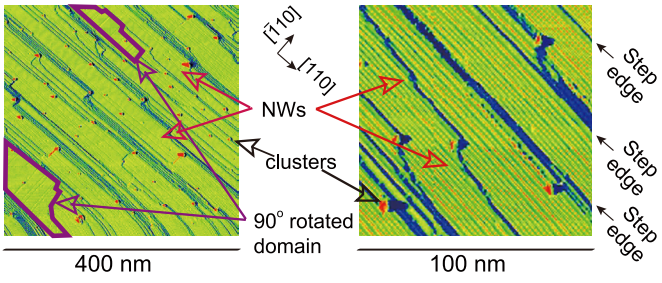

Fig. 1. STM images of Pt/Ge(001) nanowires (NW) on a vicinal Ge(001) substrate. The substrate was tilted toward the [1$\bar{1}$0] direction by 2°. Most of wide terraces are covered by the nanowires parallel to the step edges. The areas surrounded by purple lines in (left) represent minority domains. In both images, the bias voltage is 1.5 V and the tunneling current 0.5 nA.

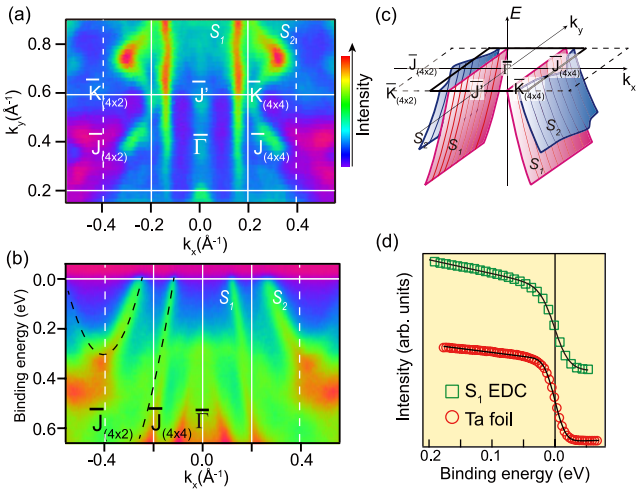

Fig. 2. (a) Constant energy ARPES intensity map at E_F of Pt/Ge(001) NWs with single-domain samples formed on the vicinal Ge(001) substrate. The photoelectron intensity is represented by color scale. (b) ARPES image taken along $\bar{\Gamma}\bar{J}$. Dashed curves represent the band structures of S_1 and S_2, which were fitted to the data. (c) Schematic illustration of the S_1 and S_2 bands. (d) Integrated energy distribution curve of S_1 near E_F over k_y in the surface Brillouin zone is compared with the results of a Ta foil.

to the phenomenology of nanowires/semiconductor systems but also a major advance for understanding the intriguing physics of the one-dimensional electrons on solid surfaces.

References

[1] Gürlu *et al.*, Appl. Phys. Lett. **83**, 4610 (2003).
[2] I. Mochizuki *et al.*, Phys. Rev. B **85**, 245438 (2012).
[3] K. Yaji *et al.*, Phys. Rev. B **87**, 241413(R) (2013).

Authors

K. Yaji, I. Mochizuki[a], S. Kim, Y. Takeichi[a], A. Harasawa, Y. Ohtsubo[b], P. Le Fèvre[b], F. Bertran[b], A. Taleb-Ibrahimi[b], A. Kakizaki, and F. Komori

[a]High Energy Accelerator Research Organization
[b]Synchrotron SOLEIL

Fabrication, Spectroscopic Characterization and Transport Properties of Aromatic Monolayers Covalently bonded to Si(111)

Yoshinobu Group

Fabrication of self-assembled monolayers (SAMs) of organic molecules on semiconductor surfaces is one of the central issues in surface science and device chemistry because of its ability to impart renewed functionalities on the surfaces. Since well-ordered and dense organic SAMs can be fabricated without severe reaction conditions and expensive equipment, organic SAMs on a semiconductor have become attractive materials that are easily accessible model systems for both fundamental scientific research and development of practical molecular devices. Among various semiconductor–organic interface structures, Si-organic molecule systems are promising candidates for future applications because of the actual proven performance of Si in today's electronics.

In this study [1], SAMs composed of aromatic molecules with different anchor groups were fabricated on the Si(111) surfaces by wet chemical reactions. We investigated the bonding structures and transport properties by spectroscopic and electrical measurements, respectively. By using simple

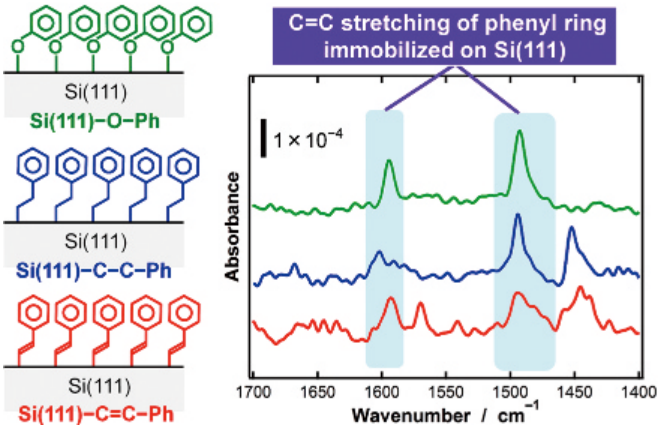

Fig. 1. (left) Schematic representations of the aromatic monolayers on Si(111) in this study [Si(111)–O–Ph (green), Si(111)–C–C–Ph (blue), and Si(111)–C=C–Ph (red)]. (right) Transmission FT-IR spectra of these Si(111)-aromatic SAMs measured at an incident angle of 60°.

aromatic molecules (phenol, styrene, and phenylacetylene) as initial precursors, we successfully fabricated aromatic SAMs covalently bonded to Si(111) surfaces through different anchor structures (Si–O–, Si–CH_2–CH_2–, and Si–CH=CH–). Transmission infrared spectra clearly indicate that the phenyl rings in the SAMs are oriented almost perpendicular to the Si surfaces. High-resolution X-ray photoelectron spectra using synchrotron radiation (KEK-PF BL13) reveal that the aromatic molecules attach to the Si surface with the surface coverage of ~ 0.5. These experimental results lead to a conclusion that the aromatic SAMs form densely packed monolayers on Si(111) using the present wet chemical methods. Judging from the current density–voltage measurements of Hg/aromatic SAM–Si(111) sandwiched structures, the "Si(111)–O–Ph" (SAM by using phenol) system shows higher conductivity compared with the long-chain alkyl SAM on Si(111).

Reference

[1] Y. Harada, T. Koitaya, K. Mukai, S. Yoshimoto, and J. Yoshinobu, J. Phys. Chem. C **117**, 7497 (2013).

Authors

Y. Harada, T. Koitaya, K. Mukai, S. Yoshimoto, and J. Yoshinobu

Visualization of "Reflectionless Tunneling" in the Superconducting Proximity Effect

Hasegawa and Kato Groups

When a superconducting material is brought into contact with a normal metal, superconducting properties penetrate into the metal. The phenomenon called proximity effect has been utilized to induce the pair correlation into various materials, including topological insulators to realize elucidating Majorana fermions.

The propagation of the proximity effect depends on the distribution of scattering centers in the normal metal, as you may expext. But curiously, it is enhanced by the presence of elastic scatters. The proximity effect is caused by the Andreev reflection at the super/normal interface, where injected electrons from the normal metal is retro-reflected as a hole whose phase is conjugated with that of the electron. Elastic scatters redirect reflected electrons/holes toward the interface, making a loop in their trajectories with the interface. Because of constructive quantum interference due to the phase conjugation, the looped trajectories enhance the probability of the Andreev reflection and consequently proximity effect. As the Andreev-reflected quasiparticles can tunnel though the interface without reflection, the enhancement is called reflectionless tunneling.

Using scanning tunneling microscopy (STM), we studied the proximity effect and the roles of the atomic-scale defects in real-space with nano-meter scale spatial resolution. The measurement was performed at 2.15 K in ultrahigh vacuum. The proximity effect was characterized via tunneling spectroscopy of a gap formed by the pair correlation at the Fermi energy. The investigated super/normal interface was formed *in situ* by creating superconducting Pb islands on a Pb-induced two-dimensional (2D) normal metal formed on a Si substrate. In Fig. 1, a topographic STM image (left) and a mapping of the corresponding conductance at the bottom of the gap, that is, zero bias conductance (ZBC) mapping (right), are shown.

In the ZBC mapping, all Pb islands are colored green, which indicates zero ZBC and good superconductivity there, and the normal metal far from the Pb islands is colored yellow, indicating no gap there. The area surrounding the Pb islands has the color of blue to red, implying a gap formation by the proximity effect. The gap propagates from the superconducting Pb islands and decays into the normal metal with the coherence length ξ of 40 nm. It is found from the mapping that the proximity effect strongly depends on the atomic structure of the interface; it is strong at the place where a Pd island is directly sitting on the 2D layer, and

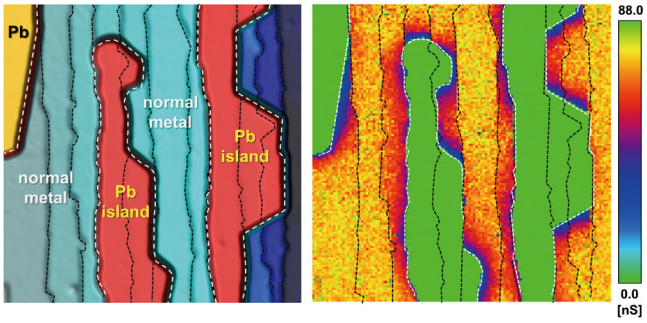

Fig. 1. (left) STM image of Pb islands on a Pb-induced two-dimensional normal metal formed on a Si substrate (1.0 μm square). The edges of the Pb islands and the steps of the normal metal layer are highlighted with white and black dotted lines, respectively. (right) The zero-bias conductance (ZBC) color map of the same area as in the topographic image.

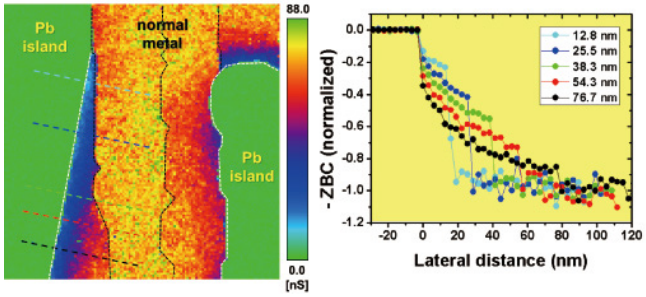

Fig. 2. (left) 400 nm × 400 nm ZBC color map taken on a confined area surrounded by the Pb island and a step edge of the normal metal layer. (right) Normalized negative ZBC profiles across the super/normal interface and the step edges measured along the colored lines drawn in the topographic image. The length written for each plot is the terrace width measured along the corresponding line.

basically no gap formation is observed at the edge of the island that coincides with the downward step of the 2D layer. The observed structural dependence can be explained by the variation of the conductivity at the super/normal interface.

We also found that the surface steps severely block the propagation, which indicate they behave as a strong potential barrier or an elastic scatter for the two-dimensional electrons. In order to find the role of the steps on the proximity effect, we investigated an area where the step is very close to the super/normal interface shown in Fig. 2 (the upper left of Fig. 1). In the wedged area whose terrace width ranges from almost 0 to 2ξ we observed the enhancement of the gap and found that deeper gap is formed on narrower terrace, as demonstrated in the right panel of Fig. 2, which shows ZBC profiles for various width terraces. Because of the real-space and cross-sectional observation, we can probe ZBC throughout the system while eliminating unwanted effects of structural defects at the super/normal interface and in the normal metal. The observed enhancement is overall consistent with the reflectionless tunneling. The dependence of the enhancement on the terrace width is, however, not explained quantitatively with the calculation based on the Usadel equation, a quasi-classical Green's function formalization. Some phenomena that are not considered in the calculation are probably involved in the enhancement of the proximity effect.

References

[1] H. Kim, S.-Z. Lin, M. J. Graf, T. Kato, and Y. Hasegawa, arXiv:1401.2602

Authors

H. Kim, S.-Z. Lin[a], M. J. Graf[a], T. Kato, and Y. Hasegawa

[a]Los Alamos National Laboratory

Ferromagnetic Josephson Junctions

Lippmaa Group

Ferromagnetism and superconductivity are generally incompatible because in conventional superconductors Cooper pairs are formed by two electrons with opposite spins, while in ferromagnets, exchange interactions align the spins parallel to each other. In our recent work, we study the possibility of a long-range supercurrent surviving in highly spin-selective materials, such as half-metals in spin filter tunnel junctions. In particular, our interest is in determining the role of magnetic disorder in promoting a spin-triplet supercurrent in a superconducting tunnel junction with a ferromagnetic insulator barrier.

The tunnel junctions (Fig. 1a) were grown by pulsed laser deposition and consisted of superconducting $La_{1.85}Sr_{0.15}CuO_4$ (LSCO) and Au/Nb/Au electrodes at the bottom and the top of the device. The gold layers were used as oxygen diffusion barriers but were superconducting due to the proximity effect. The tunnel barrier material was $Pr_{0.8}Ca_{0.2}Mn_{0.9}Sc_{0.1}O_3$ (PCMSO), which is a weakly ferromagnetic insulator. The PCMSO layer was doped with Ca to obtain the ferromagnetic insulating phase, while partial Mn substitution by Sc was used to tune the coercivity of the barrier layer and to introduce intentional magnetic disorder. An array of lithographically patterned junctions can be seen in Fig. 1b.

The tunnel junctions showed characteristic step-like

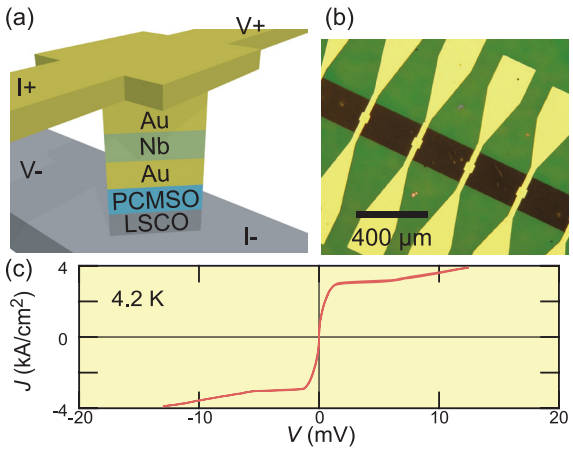

Fig. 1. (a) Schematic view of the $La_{1.85}Sr_{0.15}CuO_4$ (LSCO) / $Pr_{0.8}Ca_{0.2}Mn_{0.9}Sc_{0.1}O_3$ (PCMSO) / Au / Nb / Au junction. (b) Image of a patterned junction array. (c) Current-voltage characteristic of a junction at 4.2 K.

current-voltage characteristics below 6.9 K (Fig. 1c), limited by the superconducting transition temperature of the Au/Nb top electrode. Differential conductance spectra of the junctions showed three characteristic peaks that correspond to various quasi-particle tunneling maxima, as illustrated in Fig. 2. The spectra measured at various temperatures yielded the expected gap values for LSCO (8 to 14 meV) and Au/Nb (1.25 meV) above 4.5 K. Below this temperature, an anomalous increase of the gap energies was observed. This gap energy change was visible as an increase of the normalized critical current, $I_C R_N$ of the devices. Since the contribution of a direct leak between the *s*-wave Nb/Au top electrode and the *d*-wave LSCO bottom electrode is unlikely, we consider the possibility of scattering from magnetic disorder induced in the PCMSO barrier by the Sc doping. Magnetic disorder at a c-axis-oriented cuprate superconductor and a ferromagnet may give rise to spin-triplet supercurrent, effectively increasing the junction critical current.

The devices developed in this work allow us to probe the role of magnetic disorder at superconductor – ferromagnet interfaces, since it is possible to adjust the disorder by suitable level of Sc doping in PCMSO, while the junction characteristics can be probed as a function of an external magnetic field. Our future interest is to discern if singlet

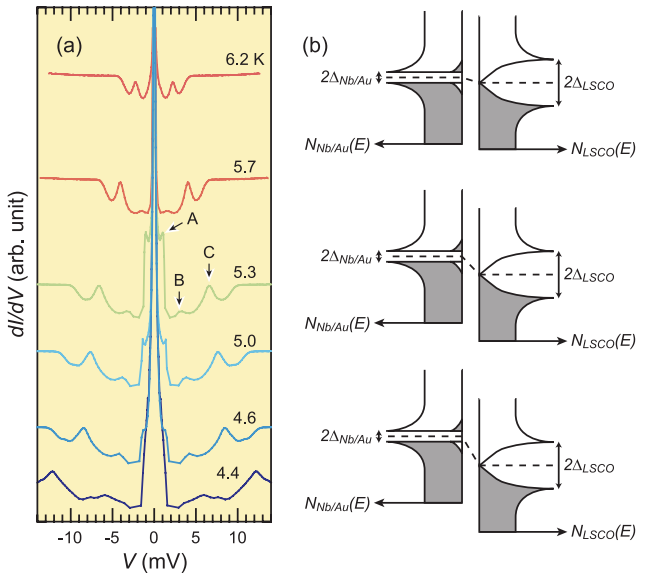

Fig. 2. (a) Differential tunneling spectra at various temperatures and (b) proposed band diagrams explaining the origins of the three peaks, A (top), B (middle), and C (bottom) in the tunneling spectra.

pairs may be stabilized by local antiferromagnetism in the barrier or if scattering into spin-triplet Cooper pairs dominates.

Athors
T. Harada[a], M. Matvejeff[b], R.Takahashi, and M. Lippmaa
[a]Max Planck Institute for Solid State Research
[b]Aalto University

Possible Kondo Physics Near a Metal-Insulator Crossover in the A-site Ordered Perovskite $CaCu_3Ir_4O_{12}$

Uwatoko Group

The interplay between localized and itinerant electrons is at the heart of many intriguing phenomena such as the heavy-fermion behavior and the unconventional superconductivity associated with a magnetic quantum critical point [1]. The archetype systems for studying such interplay are concentrated on the 4*f*/5*f*-based intermetallic compounds, which can be effectively described as a Kondo lattice consisting of a dense periodic array of f electrons interacting with the conduction-band electrons [2]. Here, we reported the realization of an analog d-electron Kondo lattice in a novel *A*-site-ordered perovskite $CaCu_3Ir_4O_{12}$, which can be synthesized only under high-pressure conditions, *e.g.* at 9 GPa and 1250 °C [3].

As shown in Fig. 1(b), the *A*-site-ordered perovskite

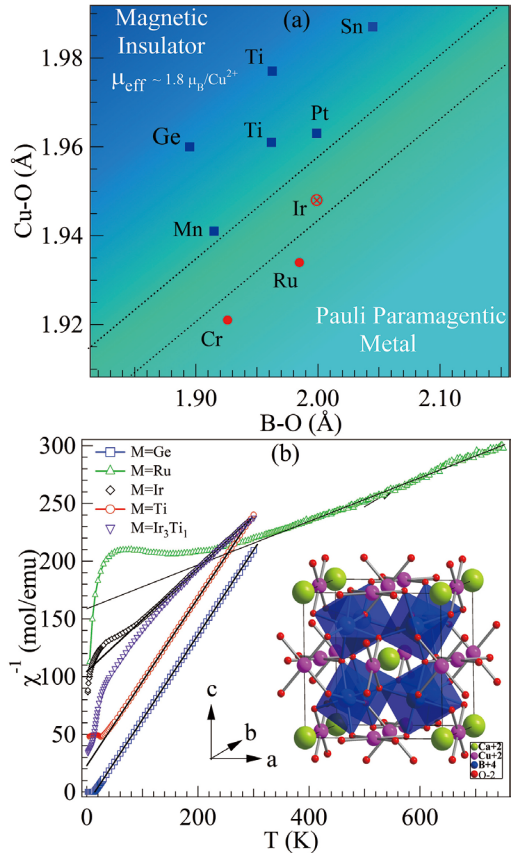

Fig. 1. (a) The Cu-O bond length in the coplanar CuO_4 versus *B*-O bond length in the octahedral BO_6 for *A*-site ordered perovskites $CaCu_3B_4O_{12}$; (b) The inverse magnetic susceptibility of several $CaCu_3B_4O_{12}$ perovskites; inset: schematic crystal structure of the *A*-site ordered perovskite.

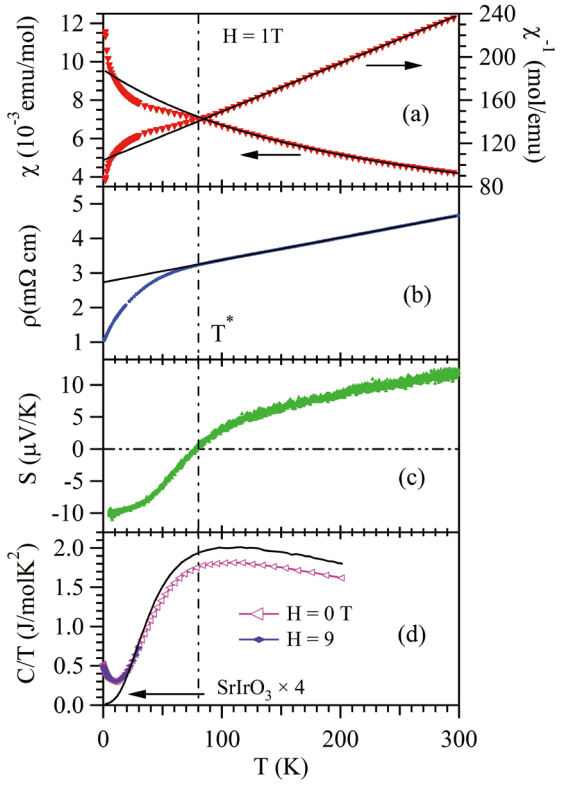

Fig. 2. Temperature dependence of (a) magnetic susceptibility $\chi(T)$ and its inverse χ^{-1}(T) measured under H = 1 T after zero-field cooling, (b) resistivity $\rho(T)$ under H = 0 T, (c) thermopower S(T), and (d) specific heat $C(T)$ under H = 0 and 9 T.

$CaCu_3B_4O_{12}$ can accommodate the Cu^{2+} and the transition-metal B^{4+} ions, respectively, in the square-planar CuO_4 and octahedral BO_6 units, in which the *d* electrons can be coupled by strong covalent mixing with shared O^{2-} ions. Depending on the B^{4+} ions, the Cu^{2+} 3*d* electrons can be tuned to be either localized or itinerant. A plot of Cu-O versus *B*-O bond length in Fig. 1(a) illustrated that the Cu^{2+} 3*d* electronic states in $CaCu_3Ir_4O_{12}$ is located right at the itinerant-to-localized boundary. In consistent with this observation, the magnetic susceptibility of $CaCu_3Ir_4O_{12}$ shown in Fig. 1(b) demonstrated a crossover from the high-temperature Curie-Weiss (CW) behavior to a low-temperature enhanced Pauli paramagnetism.

Figure 2 summarizes the physical properties of $CaCu_3Ir_4O_{12}$. The $\chi(T)$ measured at H = 1 T shows no signature of a magnetic ordering transition down to 1.8 K, but a clear deviation from the CW law below $T^* \approx$ 80 K. The susceptibility anomaly below T^* is echoed in $\rho(T)$, and also in the thermoelectric power $S(T)$. Above T^*, $\rho(T)$ follows a perfect linear T-dependence; below T^*, $\rho(T)$ exhibits a strong downward trend with no sign of a curvature change down to 0.5 K, strongly suggestive of non-Fermi-liquid behavior. Significantly, $S(T)$ also behaves anomalously, changing sign at T^* and remaining large as T approaches zero. The large thermoelectric power at low temperatures signals strongly energy-dependent quasiparticle properties. The absence of a corresponding anomaly in the specific heat $C(T)$ rules out the possibility of a second-order phase transition at T^*. Interestingly, C/T of $CaCu_3Ir_4O_{12}$ exhibits a remarkable enhancement below ~ 20 K. The absence of a corresponding enhancement in the closely related $SrIrO_3$ perovskite, which is a Pauli paramagnetic metal, indicates that this low-temperature anomaly must be associated with the Cu^{2+} 3*d* electrons or with interactions between Cu:3*d* and Ir:5*d*.

The presence of a characteristic temperature at T^* = 80

K is reminiscent of the low-temperature behavior in typical heavy-Fermion materials, and is suggestive of Kondo-like hybridization between primarily localized Cu^{2+} 3*d* electrons and the itinerant Ir 5*d* electrons below T^*. In this picture, electrons on the two sublattices are weakly coupled above T^*. The initial reduction in $\chi(T)$ relative to the extrapolated $T > T^*$ CW fit, may signal the onset of hybridization of Cu electrons with the itinerant Ir^{4+} 5*d* electrons. The quick drop of $\rho(T)$ and the sign crossover of $S(T)$ at T^* appear to confirm the emergence of a hybridization between more localized electrons on Cu and more itinerant electrons on Ir. The incorporation of the Cu^{2+} 3*d* electrons into the itinerant bands would not only enhance the density of states, but also reduce the scattering from local magnetic moments. Further evidence for the coherent incorporation of Cu local moments in the Ir bands can be found in the specific-heat measurement, leading to a strong enhanced electronic specific-heat coefficient γ = 173 mJ/mol K^2 for $CaCu_3Ir_4O_{12}$. Our results demonstrated that the *A*-site-ordered perovskites can host a broad spectrum of interesting phenomena that deserve further explorations.

References

[1] O. Stockert and F. Steglich, Annu. Res. Condens. Matter. Phys. **2,** 79 (2011).
[2] Y.-F. Yang, and D. Pines, PNAS **109**, E3060 (2012).
[3] J.-G. Cheng, J.-S. Zhou, Y.-F. Yang, H. D. Zhou, K. Matsubayashi, Y. Uwatoko, A. MacDonald, and J. B. Goodenough, Phys. Rev. Lett. **111**, 176403 (2013).

Authors

J.-G. Cheng, K. Matsubayashi, Y. Uwatoko, J.-S. Zhou[a], A. MacDonald[a], J. B. Goodenough[a], Y.-F. Yang[b], H. D. Zhou[c]

[a]University of Texas at Austin
[b]Institute of Physics Chinese Academy of Sciences
[c]University of Tennessee

Stability of Quantum Hall Ferromagnetic Phase under High Magnetic Fields in the Organic Dirac Fermion System

Osada Group

A layered organic conductor α-$(BEDT\text{-}TTF)_2I_3$ under high pressure (>1.5 GPa) is a multilayer Dirac fermion system, in which 2D massless Dirac fermion layers stack with weak interlayer coupling, and the Fermi level is fixed at the Dirac point. Such an undoped 2D Dirac fermion system shows the $\nu = 0$ quantum Hall (QH) effect at sufficiently high

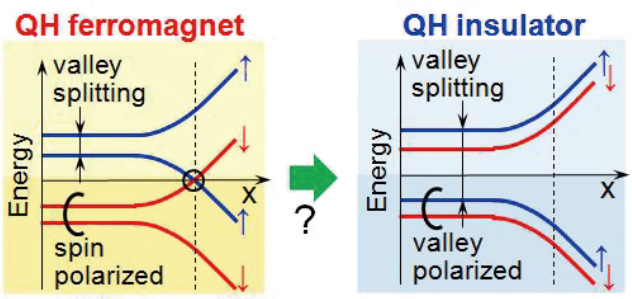

Fig. 1. Schematic energy dispersion of QH edge states in the QHF (left) and QHI (right) states. If the valley splitting becomes larger than the spin splitting in high magnetic fields, the QHF-QHI transition might occur. The helical edge channel (indicated by a circle) in the QHF phase disappears at the QHI phase.

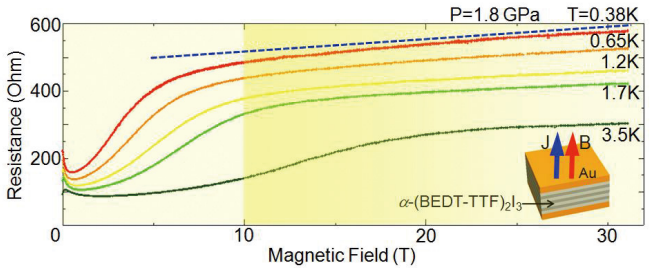

Fig. 2. High-field interlayer magnetoresistance of 2D organic Dirac fermion system α-$(BEDT\text{-}TTF)_2I_3$. No sign of the QHF-QHI transition was observed.

magnetic fields resulting from the spontaneous symmetry breaking (SSB) of four-fold (spin and valley) degeneracy of the singular $n = 0$ Landau level. Generally, two kinds of the $\nu = 0$ QH state are possible in the Dirac systems (Fig. 1): One is the QH ferromagnet (QHF) state with the metallic helical edge state consisting of a pair of $n = 0$ QH chiral edge states with opposite spin and chirality. The other is the QH insulator (QHI) state with no edge state and some real-space structure. In this way, the high-field ground state is one of the key issues of the physics of the Dirac fermion system.

In graphene, the typical 2D Dirac fermion system, the high-field ground state (the $\nu = 0$ QH state) is believed to be the QHI phase. In contrast, in α-$(BEDT\text{-}TTF)_2I_3$, the high-field ground state is considered to be the QHF phase. Its interlayer magnetoresistance shows anomalous saturation at high fields. We illustrated that this saturation resistance is scaled not by the sectional area of sample crystals but by sample perimeter. This fact directly means that the metallic surface transport is dominant in the saturating region, and it strongly suggests that the QHF phase with the metallic helical edge state is realized. However, recently, Kanoda *et al*. observed the fine structures of the NMR lineshape at higher fields (B > 15 T), which suggests the appearance of some real-space structure accompanied by the QHI. Their result shows the possibility of transition from the QHF to the QHI in higher field region.

To confirm this possibility experimentally, we performed high-field transport measurement up to 31 T using the National High Magnetic Field Laboratory at Tallahassee, USA. Since no surface transport exists in the QHI phase, rapid increase of the interlayer resistance can be expected at the QHF-QHI transition. As shown in Fig. 2, the interlayer resistance shows increase reflecting the activated bulk transport at low fields, and it switches to weak increase at higher fields up to 31 T. This saturation is caused by the surface transport via helical edge state. We can see no anomaly in the saturating region, especially around 15 T. This result means that the QHF state survives up to 31 T with no QHF-QHI transition suggested by the NMR study.

The pure QHF phase is spatially uniform state. To explain the NMR result, it might be necessary to consider the mixture of spin and valley degree of freedom.

Authors

T. Osada, M. Sato, T. Konoike, and K. Uchida

Parallelizable Multi-Worm Algorithm

Kawashima Group

Massively parallel computations open the door to many otherwise intractable problems in condensed matter physics, in particular, quantum many-body problems. Recent high-performance computers, symbolized by K-computer in Kobe, rely on a large number, as many as a million, of processors (or more precisely "cores"). Therefore, we must split the computational tasks into many bits and assigning each to one of the numerous processors. This is by no means a trivial thing to do. Often we must significantly alter algorithms to split the task in an efficient way. In other words, we must develop new parallelizable algorithms. The quantum Monte Carlo method with the worm update algorithm [1, 2] has a broad range of applicability and is one of the standard tools to treat quantum many-body problems. However, in this algorithm, update of configurations is realized via the motion of a single-point object in the whole space-time (or the lattice), making it hard to split the task.

Based on the directed-loop algorithm [2], one of the variants of the worm algorithm, we proposed a parallelizable worm algorithm, which we named the parallelizable multi-worm algorithm (PMWA). In PMWA, multiple worms are introduced by an artificial source field η and the space-time is decomposed into many domains, as illustrated in Fig. 1. Each domain is assined to a processor and typically contains 10-100 worms. We estimate physical observables by extrapolation to the $\eta = 0$ imit. Introducing multiple worms requires a different procedure from the conventional worm algorithm so as to satisfy the detailed balance condition. The migration of the worms over the domain boundaries is effectively realized through communications between domains so that the ergodicity condition is satisfied. The PMWA is applicable to the soft-core Bosons and the quantum spins as the conventional worm algorithm.

We applied the PMWA to the extended Hard-core Bose-Hubbard model on square lattice defined by

$$H = -t\sum_{(ij)} b_i^+ b_j + V\sum_{(ij)} n_i n_j - \mu\sum_i n_i - \eta\sum_i (b_i^+ + b_i)$$

where b_i is the annihilation operator at site i, t is the hopping energy, V is the nearest neighbor repulsion, and μ is the chemical potential. We established the extrapolation procedure to obtain physical quantities in the $\eta = 0$ limit. Then, we confirmed that the extrapolated PMWA result agreed with the result obtained by the conventional DLA algorithm. Figure 2(a) shows the order parameter of the Bose-Einstein

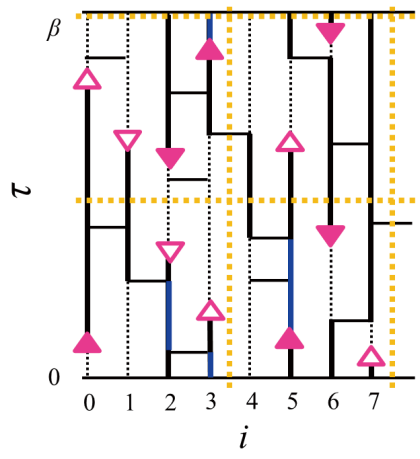

Fig. 1. Worms and worldlines in PMWA. The yellow dashed lines are the domain boundaries.

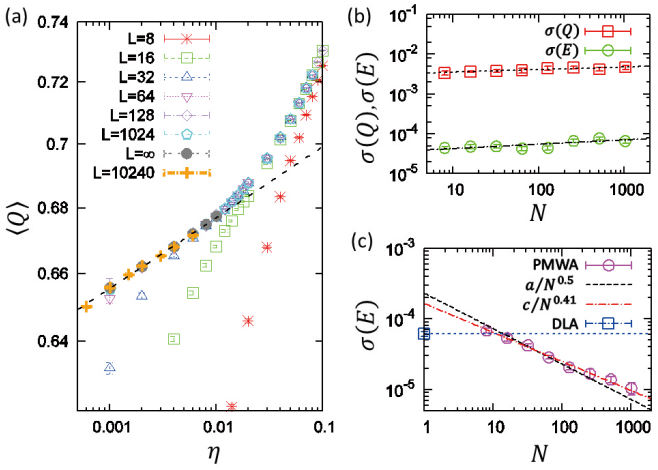

Fig. 2. (a) The order parameter of the Bose-Einstein condensate as a function of η;. (b) The standard error as a function of the number of domains with the fixed number of Monte Carlo steps. (c) The standard error as a function of the number of domains with the computational time (wall-clock time) being fixed.

condensate $Q \equiv \langle b \rangle$ as a function of η. Here we carried out simulations of the size of $L \times L \times \beta$ = 10,240×10,240×16 using 3,200 processing cores, where L is the system's linear dimension and β is the inverse temperature. This size exceeds the maximum reachable size of the conventional worm algorithm. To evaluate the parallelization efficiency of the algorithm, we measured the standard error as a function of the number of domains N. We found a very weak N-dependence for the relaxation time in the simulation with fixed number of the Monte Carlo steps (Fig. 2(b)). In addition, in comparison with the conventional DLA results, PMWA results show better accuracy in fixed wall-clock time with N>8 (Fig. 2(c)), and the difference increases as the system becomes larger.

References

[1] N. Prokof'ev, B. Svistunov, and I. Tupitsyn, Sov. Phys. JETP **87**, 310 (1998) etc.

[2] O. F. Syljuasen and A. W. Sandvik, Phys. Rev. E **66**, 046701 (2012).

[3] A. Masaki-Kato, T. Suzuki, K. Harada, S. Todo, and N. Kawashima, arXiv:1307.0328 (2013), to be published in Phys. Rev. Lett. (2014).

Authors

A. Masaki-Kato, T. Suzuki[a], K. Harada[b], S. Todo, and N. Kawashima

[a]University of Hyogo

[b]Kyoto University

Dynamic Light Scattering Microscope: Accessing Opaque Samples with High Spatial Resolution

Shibayama Group

Dynamic light scattering (DLS) is a technique for obtaining the size distribution of particles in solution. However, it cannot be applied to opaque samples. There are two types of opaque samples. One is a black sample, which is a strong light-absorbing material such as ink. In this case, scattered light is completely absorbed by the sample itself and one cannot obtain the signal. The other type is milky samples, which are strong light-scattering materials such as milk. In this case, multiple scattering is inevitable. In addition to this, poor spatial resolution sometimes also becomes a problem. There is a growing demand to investi-

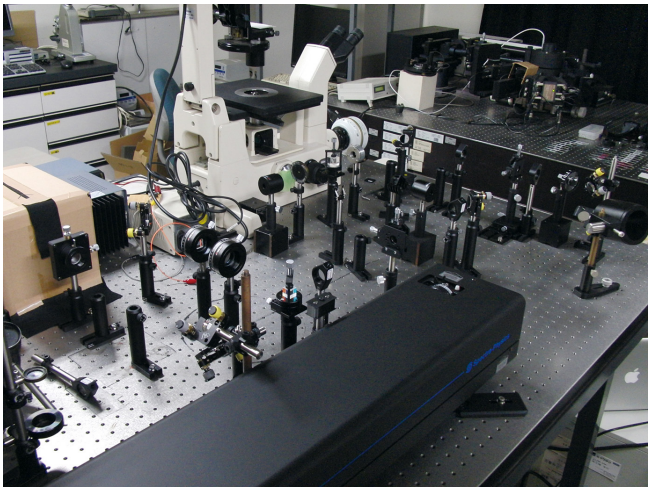

Fig. 1. Photograph of the dynamic light scattering microscope.

gate the dynamic behavior of samples with a higher spatial resolution. One such example is a tracking of material transportation in biological cells. To realize such applications, the spatial resolution needs to be near the diffraction limit. Here, we propose a new DLS technique, "DLS microscope" that mitigates the above-mentioned disadvantages (Fig. 1) [1]. The proposed DLS microscope obtains signals with a backscattering geometry. This enables us to measure opaque samples with high spatial resolution.

By using the DLS microscope, we measured the size distribution of opaque samples such as polystyrene latex and Chinese ink with changing their concentrations. Figure 2 shows the results for the polystyrene latex suspension and Chinese ink. In the case of polystyrene latex suspension, the data show the monodisperse nature. The calculated diameter shows good agreement with the nominal diameter (100 nm). Since the result for the polystyrene latex suspension shows peaks at almost the same position in all concentrations, we can conclude that the polystyrene latex suspension shows no morphology change through varying the concentration. This is consistent with the following molecular interpretation: each particle has a negative charge on the surface, and the particles repel each other keeping their form unchanged and showing Brownian motion. This result corresponds to the result obtained by using diffusing wave spectroscopy [2]. In contrast, the result for Chinese ink seems to show that the average particle size increases and the size distribution broadens at higher concentrations. However, as Chinese ink is a protective colloidal solution, the particles are considered not to aggregate. One of the possible explanations for our result is the existence of attractive interactions between colloidal particles. In other words, colloidal particles show collective motion rather than Brownian motion at higher concentrations. This consideration is supported by the fact that the viscosity of neat ink is approximately five times higher than that of water. Taking advantage of its high spatial resolution, this technique can also be readily applied to other media such as biological cells and gels.

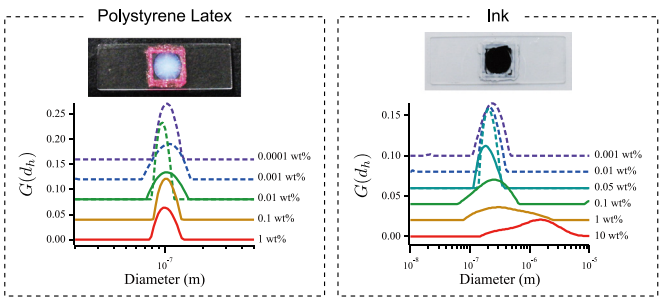

Fig. 2. (Left side) Concentration dependence of the size distribution of a polystyrene latex suspension. The nominal diameter of the polystyrene latex particles is 100 nm. The 1 - 0.01 wt%, as measured by the DLS microscope, is represented by the solid lines. The 0.01 - 0.0001 wt%, as measured by the typical DLS system, is represented by the dashed lines. (Right side) Concentration dependence of the size distribution of Chinese ink. The 10 - 0.05 wt%, as measured by the DLS microscope, is represented by the solid lines. The 0.05 - 0.001 wt%, as measured by the typical DLS system, is represented by the dashed lines.

References

[1] T. Hiroi and M. Shibayama, Opt. Express. **21**, 20260 (2013).

[2] P. Navabpour *et al*., Colloid Polym. Sci. **283**, 1025 (2005).

Authors

T. Hiroi and M. Shibayama

Magnetic Relaxation in a Tb-based Single Molecule Magnet

Yamamuro Group

A single-molecule magnet (SMM) is a metal complex that behaves as an individual nanomagnet. Each molecule, containing several metal centers with unpaired electrons, possesses a giant resultant spin. Given that the giant spin exhibits easy-axis anisotropy ($D < 0$), the magnetization reversal between the ground states with $S_z = +/-S$ is hindered by the potential barrier of DS_z^2. The traditional research subjects have been SMMs containing multiple transition metal atoms such as Mn, Fe, and Ni, while the current mainstream is shifting to lanthanide SMMs. Owing to a large contribution of angular momentum, lanthanide complexes can become SMMs containing only one or two magnetic ions. One of the central issues in lanthanide SMMs is the quantum tunneling mechanism for the magnetization reversal. In most cases, the tunneling occurs between ground states (pure tunneling process) and/or excited states (thermally assisted tunneling process). The origins of the tunneling have not been fully understood yet.

We have investigated the spin dynamics of Tb-Cu dinuclear SMM by means of neutron scattering techniques. The chemical formula of the sample is $TbCuC_{19}D_{20}N_3O_{16}$ and its molecular structure is schematically shown in the

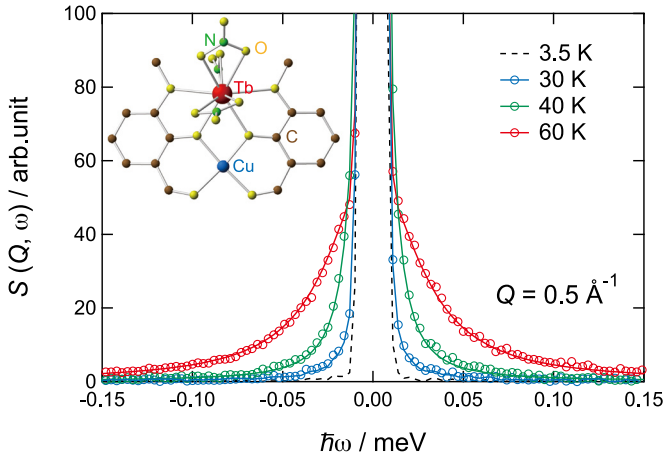

Fig. 1. Dynamic structure factors of TbCu-SMM. The data at 3.5 K represent the resolution function. The other data are fitted to the combination of delta and Lorentz functions. The inset shows the molecular structure of TbCu-SMM.

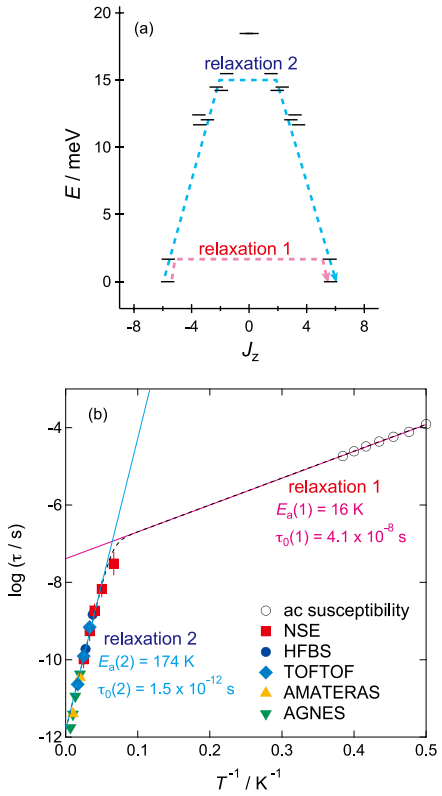

Fig. 2. (a) Calculated energy diagram as a function of z-component of the total angular momentum of Tb ion. Dashed lines represent possible relaxation processes. (b) Arrhenius plot of the relaxation times observed on the five spectrometers. The results from the ac susceptibility measurements are also shown.

inset of Fig.1. In order to reduce the contribution from the strong incoherent scattering of H atoms, the sample was fully deuterated. Only two magnetic ions, Tb^{3+}(J = 6) and Cu^{2+}(S = 1/2), are involved in a molecule. Following inelastic neutron scattering studies to determine the energy scheme [1], we investigated the magnetic relaxation by means of quasielastic neutron scattering (QENS) experiments using various spectrometers with different energy resolutions; AGNES (ΔE = 49 μeV) at JRR-3, AMATERAS (ΔE = 120 μeV) at J-PARC, TOFTOF (ΔE = 8 μeV) at FRM II (Germany), HFBS (ΔE = 0.8 μeV) and neutron spin-echo NSE (Fourier time, 0.007 < t < 12 ns) at NCNR (USA) [2]. The use of five spectrometers enables us to investigate relaxations over a wide time range between 1 ps and 100 ns.

Figure 1 shows the dynamic structure factors of Tb-Cu SMM at Q = 0.5Å^{-1} taken on the TOFTOF spectrometer. Clearly, QENS broadening was observed above 30 K. The QENS spectra were well fitted to the combination of delta and Lorentz functions. The linewidth of the Lorentzian, Γ(Q), exhibits no pronounced Q-dependence, indicating that the relaxation is of a local origin. The relaxation times were obtained from the relation τ = 1/Γ. In Fig. 2(b), we show the Arrhenius plot of relaxation times estimated from the QENS together with those from the ac magnetic susceptibility measurements. This provides a clear evidence of the existence of two distinct relaxation processes. We designate the slower relaxation as the relaxation 1 and the faster one as relaxation 2. Both relaxation processes follow the Arrhenius relation $\tau = \tau_0 \exp(\Delta E_a / k_B T)$. As for the relaxation 1, the activation energy E_a and prefactor τ_0 are estimated to be 16.0 K and 4.1 × 10^{-8} s, respectively. It should be emphasized that E_a corresponds to the excitation energy of 1.7 meV observed in the INS study [1]. We have calculated an energy diagram as a function of the z-component of the total angular momentum of the Tb ion, J_z (see Fig. 2(a)), assuming the spin Hamiltonian including ligand field anisotropy, exchange interaction between Tb^{3+} and Cu^{2+}, and hyperfine interaction. The excitation of 1.7 meV is the transition between the ground and the first excited states. We thus conclude that the magnetization reversal occurs through quantum tunneling between the pairs of degenerated excited states at 1.7 meV. This is called thermally activated tunneling process, in other words the Orbach mechanism of spin-lattice relaxation. On the other hand, the relaxation 2 detected by QENS has quite different E_a and τ_0; $E_a(2)$ = 174 K and $\tau_0(2) = 1.5 \times 10^{-12}$ s. The relaxation 2 is also of the Debye type and gets activated upon heating according to the Arrhenius law. The simplest scenario for the origin of the relaxation 2 is that the relaxation 2 takes place through the tunneling between higher excited states. The activation energy of 174 K (= 15 meV) roughly corresponds to the higher energy level as seen in the energy diagram in Fig. 2(a).

This is the first successful QENS work to observe magnetic relaxation in SMM. The use of QENS can open a new window into the study of relaxation processes in the class of SMMs.

References

[1] M. Kofu, O. Yamamuro, T. Kajiwara, Y. Yoshimura, M. Nakano, K. Nakajima, S. Ohira-Kawamura, T. Kikuchi, and Y. Inamura, Phys. Rev. B **88**, 064405 (2013).

[2] M. Kofu, T. Kajiwara, J. S. Gardner, G. G. Simeoni, M. Tyagi, A. Faraone, K. Nakajima, S. Ohira-Kawamura, M. Nakano, and O. Yamamuro, Chem. Phys. **427**, 147 (2013).

Authors

M. Kofu, T. Kajiwara[a], G. G. Simeoni[b], and O. Yamamuro

[a]Nara Wemen's University

[b]Technical University of Munich

Nano-magnetism in Relaxor Magnet $LuFeCoO_4$

Masuda Group

Dielectric property exhibiting an enhanced permittivity in wide temperature range is known as relaxor ferroelectricity and it has attracted great interest in the field of basic and applied physics. In the relaxor system Polar Nanoregions (PNRs), where coherent polarizations in nano-scale domains are randomly oriented in the bulk crystal, play important role. So far disordered perovskite oxides such as $Pb(Mg_{1/3}Nb_{2/3})O_3$, $Pb(Sc_{1/2}Ta_{1/2})O_3$, etc., have been extensively studied [1] and all of them are purely dielectric and non-magnetic. Here natural question arises: what would happen if the relaxor system contains magnetic ions? One of our group members answered to the question in his pioneering work on a relaxor magnet, $2/3BiFeO_3$-$1/3BaTiO_3$ [2]; appearance of a new type of nano-magnetism where superparamagnetic moments are induced limitedly inside the PNRs. For further understanding of relaxor magnets we study a new compound $LuFeCoO_4$ by combination of bulk properties measurements and neutron diffraction technique. Our study reveals the relationship between PNRs and magnetic correlation, and establishes the magnetic and dielectric phase diagrams of the relaxor magnet as shown in Fig. 1(a) [3].

$LuFeCoO_4$ is a two-dimensional (2D) triangular spin

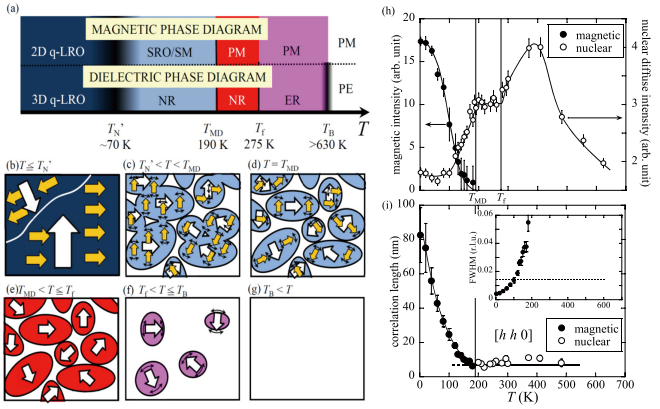

Fig. 1. (a) Magnetic phase diagram (upper panel) and dielectric phase diagram (lower panel). PM, SM, NR, ER, and PE mean paramagnetism, superparamagnetism, nonergodic relaxor, ergodic relaxor, and paraelectric, respectively. (b)-(g) The relationship between PNR and magnetic correlation at various temperatures. White arrows are electric polarization and yellow arrow are weak-ferromagnetic moments. (h) Temperature dependence of magnetic and nuclear diffuse intensities. (i) The temperature dependencies of magnetic and nuclear correlations.

system where Fe^{3+} and Co^{2+} ions are randomly positioned on the vertices of the triangles. Temperature dependence of the permittivity constant showed a typical behavior of a conventional relaxor. The result suggested the existence of PNRs and it is supported by neutron diffuse scattering. Magnetic susceptibility showed a weak-ferromagnetic component and magnetization showed superparamagnetic behavior at T < 190 K. With further decreasing the temperature the susceptibility showed a well-defined anomaly at 70 K and the magnetization showed hysteretic behavior at the base temperature, indicating a realization of magnetic order with a weak-ferromagnetic component.

The nuclear scattering results at T > 190 K in Fig. 1(h) show typical behavior of relaxor systems. At 190 K < T < 275 K, the PNRs are freezed and static. With decreasing the temperature at T = 190 K the nuclear diffuse intensity begins to decrease and simultaneously the magnetic peak appears. These results mean that the size of the PNRs increases and, synchronizedly, magnetic correlation develops. The magnetic correlation length at 190 K is 7 nm and it is the same as that of nuclear scattering as shown in Fig. 1(i).

Based on the bulk property measurements and neutron diffraction experiments, we propose a superparamagnetic model that a weak ferromagnetic correlation is, in the temperature range of 190 K < T, developed in the crystallographic c plane inside the PNRs as schematized in Fig. 1(d). Outside the PNRs the nuclear correlation is incoherent and so is the magnetic correlation. Spin moments in the PNRs behave as superparamagnetic moments and those outside the PNRs do as conventional paramagnetic spins. At the temperature T_{MD} ~ 190 K the magnetic correlation achieves long-ranged inside the PNRs. With decreasing the temperature the domain size of PNR increases and consequently the accompanied magnetic domain increases as described in Fig. 1(c). At the $T_{N'}$ = 70 K a magnetic correlation in 2D and dielectric correlation in 3D are both in quasi-long-range order as schematized in Fig. 1(b). Meanwhile at $T \geq T_{MD}$ the magnetic order is absent as shown in Figs. 1(e)-(g). The proposed model consistently explains both bulk properties and neutron scattering results.

References

[1] A.A. Bokov and Z.-G. Ye, J. Mater. Sci. **41**, 31 (2006).
[2] M. Soda *et al*., J. Phys. Soc. Jpn. **80**, 043705 (2011).
[3] M. Soda *et al*., submitted to Phys Rev. B.

3D Liner Imploding Process in the Electro-Magnetic Flux Compression

Takeyama Group

The electromagnetic flux compression (EMFC) technique in ISSP has been established to generate magnetic fields up to 730 T [1], which is the world strongest magnetic field in an indoor experiment. There, a metallic cylinder called the "liner" is subjected to the inductive electromagnetic force from a primary coil, and the initial magnetic field (~4 T) is compressed by an imploding liner within a few microseconds before the magnet destruction. Owing to the high reproducibility in its operation of the EMFC technique, solid-state physics experiments are nowadays available in ultra-high magnetic fields of up to 700 T at room temperature and up to 600 T at temperatures as low as 5 K. For solid-state physics experiments performed under ultra-high magnetic fields, the particularly important issues are (a) high precision of the magnetic field intensity, (b) the spatial uniformity of the magnetic field, and (c) appropriate bore at a peak magnetic field. For issue (a), the magnetic field intensity was recently verified to have a precision of 3 % up to 500 T, by calibrating with the Faraday rotation measurement on optical glasses [2]. For issues (b) and (c), detailed knowledge of dynamical magnetic-flux compression processes is required, for which computer simulation can be a powerful tool. Thus, we clarified the relationship between the liner's imploding process and the spatiotemporal distribution of the magnetic field intensity, by comparing with the simulation [3].

In Fig. 1(a), the solid curve is the magnetic field intensity curve (hereafter termed as the B-t curve) at z = 0. We adopted the liner of 50 mm length (L_{lin}, illustrated in the inset) and of 1.5 mm thickness. A multi-probe with an eight pick-up coils were set along the magnetic field axis (defined as the z-axis) at the center of the imploding liner, and the spatial distribution of the magnetic field intensity was simultaneously measured in a single shot The magnetic field's profile in the z direction, $B(z)$, was shown in Fig. 1(b). The field homogeneity was thus successfully determined for the first time in the EMFC experiment. Up to 500 T, the field homogeneity was estimated as good as the measurement error (~3 %) at z = ±1 mm, which has proven to be sufficiently good for the general solid-state physics measurements.

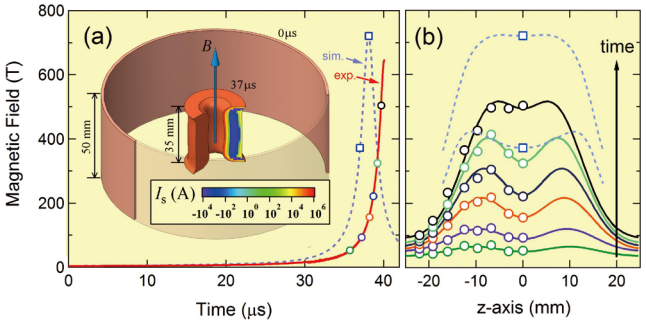

Fig. 1. (a) Magnetic field curves of the experiment (the solid curve, L_{lin} = 50 mm) and the simulation (the dashed curve, L_{lin} = 35 mm). The inset illustrates the liner's shape. For t = 0 μs, we show the liner used in the experiment (L_{lin} = 50 mm). For t = 37 μs, the simulated imploding liner in case of L_{lin} = 35 mm deforms into a barrel-like shape. The color map indicates the secondary current intensity, I_s, induced in the liner. (b) Spatial profiles of magnetic field intensity along the magnetic field axis at each time, which corresponds with the open symbols in (a). The solid-curves are the fitting of two Gaussian functions for the experimental data, and the dashed curves are the simulated spatial profiles in case of L_{lin} = 35 mm.

Two-hump structure of $B(z)$ in Fig. 1(b) is hardly explained by the mesh modeling of liner's dynamics developed by Miura and Nakao [4]. In Ref. 4, the liner's thickness was assumed to keep uniform along the z direction during the implosion. However, their model is far from accuracy in describing the real situation and is oversimplified. Therefore, we revised the simulation by independently calculating the dynamics of the liner mesh with its respective z coordinate, which allows us to obtain a nonuniform liner deformation.

The dashed curves in Figs. 1(a) and 1(b) are the simulation result in case of L_{lin} = 35 mm. The length of the primary coil (L_{pri}) is set to be 45 mm. The simulated liner's shape at 37 μs is illustrated in the inset of Fig. 1(a), and the color map indicates the secondary current intensity, I_s, induced in the liner. The barrel-like deformation of liner's inner wall shown in Fig. 1(a) induces the two hump structure of $B(z)$ in Fig. 1(b). Note that the liner's barrel-like deformation only takes place when $L_{lin} < L_{pri}$, whereas L_{lin} (50 mm) > L_{pri} (45 mm) at t = 0 μs in the real experiment. This fact implies a three-dimensional implosion process associated with a compression of the liner along the z-axis. The present work has pointed out that a three-dimensional analysis of an imploding liner is of particular importance for further record-breaking higher magnetic field in the EMFC, and for an increased controllability as well as a higher precision in the solid-state physics measurements.

References

[1] S. Takeyama and E. Kojima, J. Phys. D: Appl. Phys. **44**, 425003 (2011).
[2] D. Nakamura *et al*., Rev. Sci. Instrum. **84**, 044702 (2013).
[3] D. Nakamura, H. Sawabe and S. Takeyama, Rev. Sci. Instrum. **85**, 036102 (2014).
[4] N. Miura and K. Nakao, Jpn. J. Appl. Phys. **29**, 1580 (1990).

Authors

D. Nakamura and S. Takeyama

Heat Pulse Measurements of Specific Heat in Pulsed Magnetic Fields

Kindo Group

Measurements of the specific heat (C_p) in magnetic fields have been widely used to investigate fundamental properties of a material. Although several attempts to provide specific heat data at high magnetic field have been made, experiments in pulsed magnets are subject to strong constrains that arise from the short timescale of the measurements. Therefore, calorimetric studies have all been limited to the magnetic field range accessible to continuous magnets (dc magnets), with very few exceptions of pulsed magnets having an unusually long (>250 ms) pulse field duration [1,2]. In this context, we have developed, for the first time, a calorimeter that can operate in short pulse duration of less than 50 ms [3].

We attempt to obtain a quick thermal response by reducing the physical size of the calorimeter. Our calorimeter consists of a $Au_{16}Ge_{84}$ thin-film thermometer, a $Ni_{50}Cr_{50}$ thin-film heater, 100 μm diameter Constantan relaxation wires, and a quartz thermal bath. The eliminations of a bulk thermometer and a bulk heater lead to a quick monitoring of the temperature and enable us to study thermodynamic properties, such as C_p and magnetocaloric effect (MCE), in the 36 ms pulsed magnet that is commonly used to reach fields above 50 T. As a test of our thin-film based calorimeter, we have measured the C_p of slab-shaped $Cu_3Mo_2O_9$ single crystalline samples (0.10 mg (sample 1) and 0.0285 mg (sample 2)) between 3 and 20 K in pulsed magnetic fields up to ~56 T.

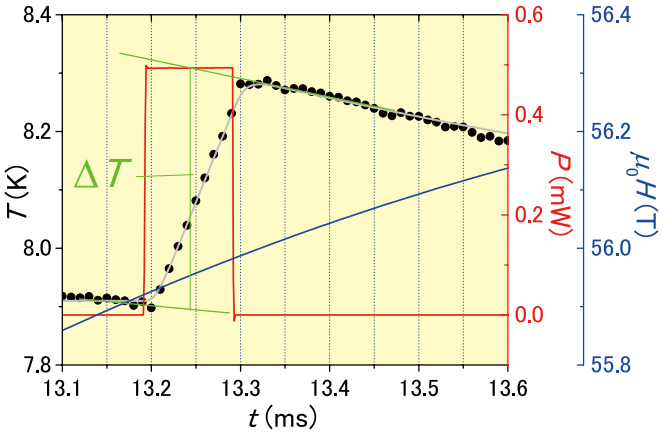

Fig. 1. Time dependence of the temperature (black dots), the power of the heat pulse (red), and the field profile (blue) during the 36 ms pulsed magnetic field. Gray curve represents a fit obtained with a simple heat equation.

Figure 1 shows the time dependence of sample temperature (black curve) during a specific heat measurement in the presence of 56 T pulsed magnetic fields. During the application of square heat pulse (red curve), the sample temperature linearly increased, and immediately after the heat pulse a clear step in temperature was observed. The short time scale of measurement (~0.5 ms) significantly reduces the uncertainty in magnetic field (blue curve); 0.2% of the applied field (56.0 ± 0.1 T) for observing a single temperature step. Since the step-like temperature change is the ideal situation for the heat pulse calorimetry, the change of the temperature (ΔT) can be estimated by the linear extrapolation (green lines in Fig. 1(a)), and the ΔQ is obtained by integrating the $P(t)$ curve. The molar specific heat was calculated by $C_p = \Delta Q \Delta T^{-1} m^{-1} M$, where m and M are the sample mass and the molar weight, respectively, and its temperature dependence was plotted in Fig. 2.

Figure 2 shows the $C_p(T)$ of sample 1 (black dots) and sample 2 (blue crosses) in various magnetic fields are shown together with PPMS data measured at 0, 7 and 13 T. $C_p(T)$

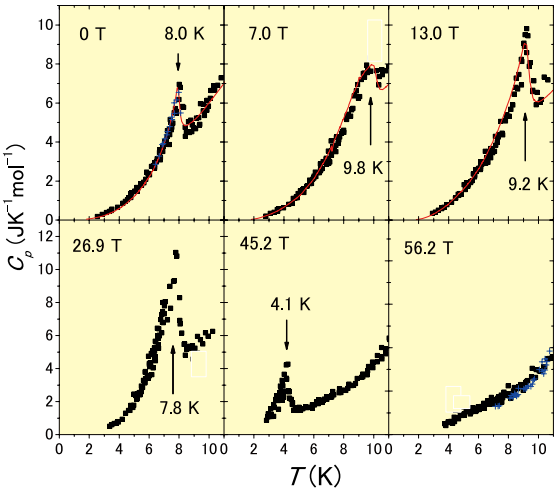

Fig. 2. A comparison of the specific heat data from the heat-pulse calorimeter (sample 1; black squares and sample 2; blue crosses) with those from the PPMS (red curves) near the phase transition in $Cu_3Mo_2O_9$. Arrows indicates the peak temperature in specific heat.

show λ-type pronounced peak and its peak temperature and the size of the anomaly varies as the applied magnetic field changes. Although the point-to-point scatter obtained from the present set-up is more than that of PPMS (red curve), the over-all temperature dependence of C_p, including the peak shape and its absolute value, agree well with the data measured in PPMS. We estimate that the absolute accuracy of the measurement is better than ±10% for temperature range from 3 to 20 K. The quantitative agreement between two sets of data shows that the experiment we are doing in pulsed field is the same as the experiments we have been doing in dc fields. The resultant $C_p(T)$ data can be analyzed in the conventional way to determine the entropy, specific heat exponent, and possibly the order of the phase transition.

We have developed an effective calorimeter for use in a pulsed magnetic field up to ~56 T and tested their performance with $Cu_3Mo_2O_9$ single crystalline samples. For $Cu_3Mo_2O_9$, this system exhibits an overall accuracy of better than ±10% for entire temperatures range of 3 to 20 K. This technique is now open to users of International Megagauss Science Laboratory.

References

[1] M. Jaime *et al*., Nature **405**, 160 (2000).
[2] Y. Kohama, C. Marcenat, T. Klein, and M. Jaime, Rev. Sci. Instrum. **81**, 104902 (2010).
[3] Y. Kohama, Y. Hashimoto, S. Katsumoto, M. Tokunaga, and K. Kindo, Meas. Sci. Technol. **24**, 11505 (2013). (IOP select)

Authors

Y. Kohama, Y. Hashimoto, S. Katsumoto, M. Tokunaga, and K. Kindo

Electronic Phase Transitions of Graphite in the Quasi-Quantum Limit State

Tokunaga and Kindo Groups

The quantum limit state, where all carriers populate the lowest Landau level, exhibits various anomalous phenomena because of the strong correlation acting on the carriers confined by magnetic fields. This state can be realized only in extremely high magnetic fields, the order of 10^4 T, in ordinary metals.

Graphite is a semimetal having a small number of electrons and holes (~ 3×10^{18} cm^{-3} for each) and goes into the quasi-quantum limit state, where only the lowest electron-like (Landau index $n = 0$, spin ↑ and ↓) and hole-like ($n = -1$, ↑ and ↓) subbands are populated in magnetic fields above 7.4 T applied along the c-axis. With further increasing the field, emergence and collapse of a density wave state has been claimed through measurements of in-plane (ρ_{xx}) and out-of-plane (ρ_{zz}) resistivity [1]. In addition, recent magnetoresistance measurements up to 80 T suggested emergence and collapse of another density wave state at 53 T and 75 T, respectively [2]. The actual nesting vector in these density wave states and also the underlying structure of the subbands, however, remain unclear as yet because of the limited experimental technique available above 25 T.

We studied Hall resistivity (ρ_{xy}) and magnetization of graphite single crystals in pulsed high magnetic fields [3]. As the main feature of the results, the ρ_{xy} becomes almost zero as the field approaches 53 T, where ρ_{xx} and ρ_{zz} show anoma-

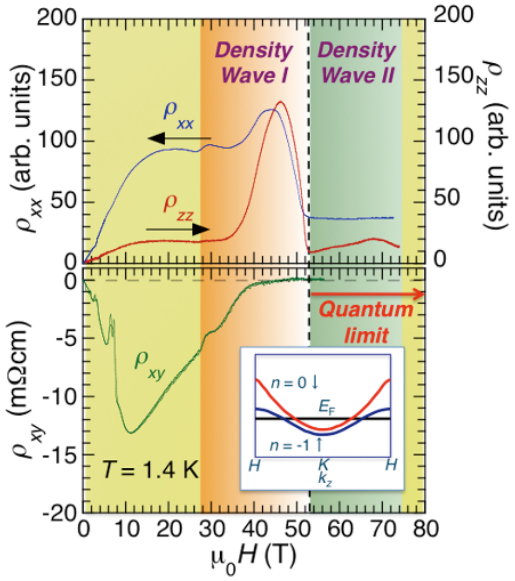

Fig. 1. (upper) In-plane (ρ_{xx}) and out-of-plane (ρ_{zz}) resistivity of graphite single crystals as a function of magnetic field applied along the c-axis at temperature of 1.4 K. (lower) Magnetic field dependence of in-plane Hall resistivity (ρ_{xy}) of graphite at 1.4 K. The colored areas represent different electronic phases suggested by transport measurements. The inset of the lower panel shows schematic illustration of the dispersion curves of the populated subbands above 53 T.

lies as shown in Fig. 1. In the microscopic point of view, the Hall resistance is given by summation of the matrix elements of the current operator between the states having different Landau indices $\Delta n = 1$ and, hence, sensitive to the whole dispersion curves of the relevant subbands. The almost zero Hall resistance seems consistent with the existence of two populated subbands ($n = 0\downarrow$ and $n = -1\uparrow$) [1] rather than the less-symmetric three subband model ($n = 0\uparrow$, $n = 0\downarrow$ and $n = -1\uparrow$) [2]. Thereby, the quantum limit state likely emerges above 53 T. In this quantum limit state, density wave can be formed by the nesting between the Fermi points of the $n = 0\downarrow$ and $n = -1\uparrow$ subbands, which is equivalent to the BCS-like pairing state of excitons. Further studies are needed to clarify the nature of the additional phase transition at 75 T in this quantum limit state.

References

[1] H. Yaguchi and J. Singleton, J. Phys.: Condens. Matter **21**, 344207 (2009).
[2] B. Fauqué *et al.,* Phys. Rev. Lett. **110**, 266601 (2013).
[3] K. Akiba *et al.*, submitted to J. Phys. Soc. Jpn.

Authors

K. Akiba, A. Miyake, H. Yaguchi[a], A. Matsuo, K. Kindo, and M. Tokunaga
[a]Tokyo University of Science

Ultrafast Photo-Induced Transition of an Insulating VO_2 Thin Film into a Non-Rutile Metallic State

Shin Group

Vanadium dioxide (VO_2) is an exemplary strongly correlated material known for its dramatic insulator-to-metal transition around room temperature (Fig. 1(a)). The phase transition can also be triggered by external stimuli such as electric gating and light irradiation. VO_2 thus provides an interesting platform for novel functionalities. By using time-

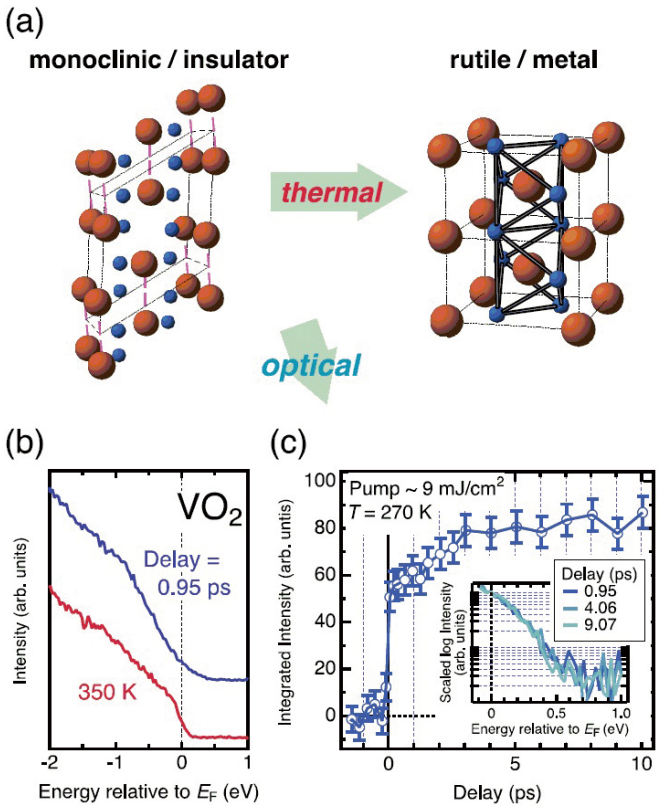

Fig. 1. Insulator-to-metal transition of VO_2. (a) Structural change from monoclinic insulating phase to rutile metal phase upon the thermal transition. (b) Time-resolve spectrum at delay = 0.95 ps (F ~ 9 mJ/cm^2, 270 K) compared with a static photoemission spectrum of a rutile metallic state recorded at 350 K. (c) Time evolution of spectral weight over [-0.2, 0.2 eV]. The inset shows the unoccupied side of the spectra for delay = 0.95, 4.05, 9.07 ps in the logarithmic scale.

resolved photoemission spectroscopy (TrPES) implemented by a high-harmonic generation method, we investigated the ultrafast photo-induced transition of VO_2, and provide insights into the non-equilibrium dynamics governed by strong correlations.

The valence-band spectrum of a VO_2 thin film was monitored in a pump-and-probe TrPES configuration. A metallic state emerged when the sample was impinged by a 170-fs pulse above a critical fluence F = 6 mJ/cm^2, which was directly evidenced by the ultrafast increase of the spectral weight at the Fermi level (E_F). The transition was accompanied by a spectral-weight transfer on a 1-eV scale characteristic of strong electron correlations. The photo-induced metallic state exhibited a unique spectrum that tails up to ~0.4 eV above E_F. This indicates that the emergent metallic state is different from the rutile state (Fig. 1(b)). After the impulsive impact, the spectral weight at E_F further increased until ~3 ps (Fig. 1(c), inset), indicating that the metallic state grew proliferatively. The ~0.4-eV tail also persisted for > 3 ps, the behavior of which cannot be explained by the photo-response of typical Mott insulators that relaxes within ~1 ps. These observations emphasize the importance of non-electronic degrees of freedom in the photo-induced dynamics of VO_2.

Reference

[1] R. Yoshida, T. Yamamoto, Y. Ishida, H. Nagao, T. Otsuka, K. Saeki, Y. Muraoka, R. Eguchi, K. Ishizaka, T. Kiss, S. Watanabe, T. Kanai, J. Itatani, and S. Shin, Phys. Rev. B **89**, 205114 (2014).

Authors

R. Yoshida, T. Yamamoto, Y. Ishida, H. Nagao[a], T. Otsuka[a], K. Saeki[a], Y. Muraoka[a], R. Eguchi[a], K. Ishizaka, T. Kiss, S. Watanabe, T. Kanai, J. Itatani, and S. Shin
[a]Okayama University

Development of the Polarization Control Segmented Cross Undulator at SPring-8 BL07LSU

I. Matsuda, Harada, and Shin Groups

Synchrotron-based soft X-ray spectroscopy has proven to be a powerful experimental technique for studying the atomic, molecular and electronic structures of materials. The energy range of soft X-rays covers the *K*-edge absorption of the most abundant elements on Earth (*e.g.* C, N, O, Si) and the *L*-edge absorption of the industrially important transition metals (Ti, V, Cr, Mn, Fe, Co, Ni, Cu and Zn). Soft X-ray spectroscopy has many unique characteristics, such as element specificity, chemical specificity and surface sensitivity. Furthermore, responses of a matter with different light polarization determine orbitals of the electronic states in solids, configurations of molecules on a surface, and spin/orbital magnetic moments of magnetic atoms. These properties make them versatile for application in a wide range of scientific fields including surface chemistry, environmental science and magnetism. Therefore, developments of polarization control soft X-ray sources have been one of the significant issues in condensed matter physics.

Recently, we have constructed a new soft X-ray beamline, BL07LSU, at SPring-8 to perform advanced soft X-ray spectroscopy for materials science. To realize the state-of-the-art performance, a novel segmented cross undulator (SCU) was developed and adopted as a soft X-ray light source. Figure 1 shows schematic drawing and photograph of the SCU. It consists of eight undulator segments and seven phase shifters (PS), and its total length is 27 m. Four segments generate horizontally linearly polarized radiation at the fundamental radiation (Figure-8 undulator), and the other four segments generate vertically linearly polarized radiation (Figure-∞ undulator). The horizontal and vertical undulator segments are placed alternately. Circular or tilted linearly polarized light can be obtained by superposing horizontally and vertically linearly polarized radiation, and the helicity of the circularly polarized radiation, for example, can be changed by the PSs. The PSs adjust the relative phase of the undulator radiation emitted from each segment by changing the path length of the electron orbit between segments with a local orbit bump. Linear polarization, P_L, and circular polarization, P_C, are evaluated by the rotating analyzer ellipsometry using the multilayer mirrors. The degrees of linear polarization (P_L) from four horizontal or four vertical segments are both 1.00. The degree of circular polarization (P_C) from four horizontal and four vertical

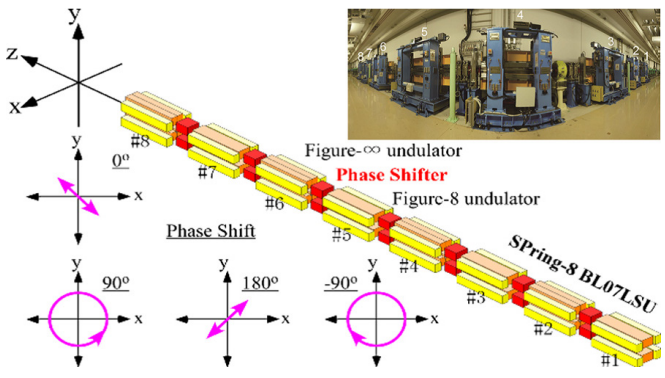

Fig. 1. Schematic and photograph of a novel segmented cross undulator at SPring-8 BL07LSU that generates polarization controlled soft X-ray.

segments are - 0.94 and 0.93 for left- and right-handed circularly polarized light, respectively.

The degree of polarization at SPring-8 BL07LSU is high enough to perform various soft X-ray spectroscopy using light polarization, such near-edge X-ray fine structure, X-ray magnetic circular dichroism, X-ray magneto-optical Kerr effect, and resonant soft X-ray diffraction. Moreover, the beamline optics and the experimental stations allow users to carry out the experiments also at small region (70 nm), with time resolutions (50 ps), and with high energy resolution (> 10,000).

Reference
[1] S. Yamamoto, Y. Senba, T. Tanaka, H. Ohashi, T. Hirono, H. Kimura, M. Fujisawa, J. Miyawaki, A. Harasawa, T. Seike, S. Takahashi, N. Nariyama, T. Matsushita, M. Takeuchi, T. Ohata, Y. Furukawa, K. Takeshita, S. Goto, Y. Harada, S. Shin, H. Kitamura, A. Kakizaki, M. Oshima, and I. Matsuda, Journal of Synchrotron Radiation **21**, 352 (2014).

Authors
I. Matsuda, S. Yamamoto, Y. Harada, and S. Shin

Discovery of a Giant Kerr Rotation in a Ferromagnetic Transition Metal by M-edge Resonant Magneto-Optic Kerr Effect

I. Matsuda and Shin Groups

Magneto-optical effects are one of the central topics in condensed matter physics. The effects have been used to study magnetism and spin transport in materials. Many experiments with the magneto-optical Kerr effect (MOKE) have been performed using linearly polarized laser light of a single wavelength typically in the visible region. Recently, there has been remarkable progress in new-generation light sources, such as the X-ray free-electron laser (FEL) and the high-harmonic generation (HHG) laser. These new monochromatic lasers have ultra-short pulse widths and tunable photon energies ranging from the extended violet to the X-ray region. Thus, MOKE measurements with photon energy tuned at the absorption edge (so-called resonant MOKE or RMOKE) are of considerable interest. Measurements with the new-generation light sources are expected to be element-specific and to trace spin dynamics in real time via time-resolved measurements.

In the present research, we have studied the Kerr rotation angle and ellipticity in the RMOKE at photon energies corresponding to the M-shell absorption edge of transition metal. We investigated the RMOKE in the well-known nickel film both theoretically and experimentally. The simulation was carried out with resonant scattering theory based on the Kramers-Heisenberg formula. The predicted Kerr rotation angle indicated a large MOKE (> 10˚). Then, the large Kerr rotation angle was confirmed by rotating analyzer ellipsometry using vacuum ultraviolet (VUV) synchrotron radiation at KEK PF BL-18A. Figure 1 compares experimentally measured and calculated variations of θ_k with photon energy. The experiment reproduced large θ_k values (~10 degree) at the absorption edge: the overall features are in good agreement with the calculations, where the model parameter set has been independently determined with other core-level spectroscopies.

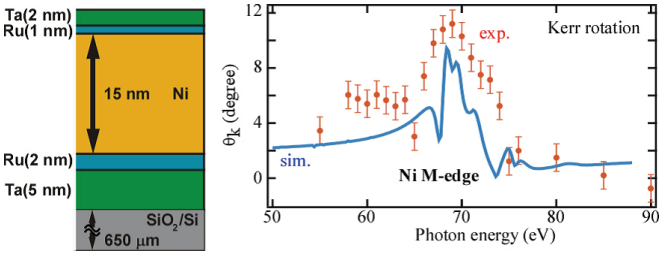

Fig. 1. Photon energy dependence of the Kerr rotation angle, θ_k, of the Ni film calculated with the resonant scattering theory (sim.) and measured experimentally with VUV synchrotron radiation (exp.). Measurement was performed at room temperature under a magnetic field of B = ± 0.47 T.

Since the RMOKE measurement is inherently element specific and is a photon-in and photon-out experiment, it is able to probe spin states of selected elements in complicated magnetic materials under external electromagnetic fields. Moreover, we observed a large Kerr rotation angle (> 10˚) in the RMOKE, which is much larger than angles (<1˚) typically found for the MOKE with visible light. Conventional MOKE measurement has always required lock-in amplifier techniques to obtain a high enough signal-to-noise ratio. However, the large Kerr rotation angle in the RMOKE we observed does not require such techniques. This advantage allows us to detect the magnetism or spin dynamics of a very small amount of the magnetic element in a material, such as a dilute magnetic semiconductor, or to measure very small structure, such as the magnetic nanostructure on a surface. This feature makes it possible to trace these ultrafast spin dynamics in terms of individual chemical species in *real time* when combined with FEL or HHG lasers.

Reference
[1] Sh. Yamamoto, M. Taguchi, M. Fujisawa, R. Hobara, S. Yamamoto, K. Yaji, T. Nakamura, K. Fujikawa, R. Yukawa, T. Togashi, M. Yabashi, M. Tsunoda, S. Shin, and I. Matsuda, Phys. Rev. B **89**, 064423 (2014).

Authors
I. Matsuda, Sh. Yamamoto, T. Nakamura[a], and S. Shin
[a]Japan Synchrotron Radiation Research Institute/SPring-8

Ultra-Broad Mode-Spacing Optical Frequency Comb

Kobayashi Group

A mode-locked oscillator produces bunch of regularly spaced longitudinal modes in an optical frequency region. It is called as an optical frequency comb. When the frequency comb was invented, it was regarded as a dream light source since one oscillator produces tens of thousands modes, corresponding to thousands of ultra-narrow linewidth cw lasers. Many people said that cw lasers were no longer necessary since making the mode-locked laser was easier than making very stable cw lasers. However, this story was not correct. One could not chose one comb tooth from neighboring modes because the mode spacing was too small to pick by using any dispersive optics. The mode-spacing is a repetition rate of the mode-locked (ML) oscillator, the high-repetition rate then makes broad mode spacing. The repetition rate of the ML laser is determined by the cavity length since only one pulse is propagating in a cavity. The smaller cavity then

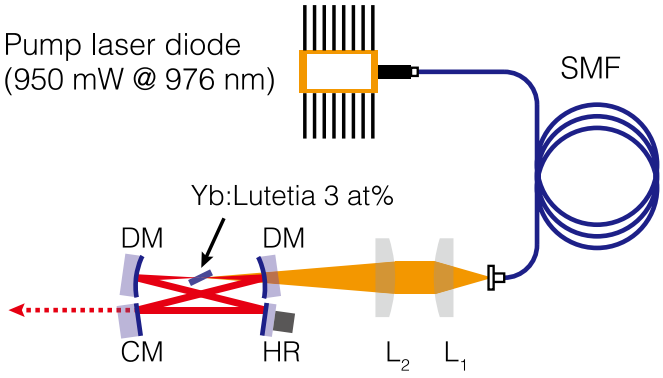

Fig. 1. Schematic of the experimental setup. DMs, dichroic mirrors; CM, chirp-compensation mirror; HR, high reflection mirror; L1 and L2, lenses.

produces the broader mode-spacing optical frequency comb. Another direction is to make higher resolution spectrometer or spectrograph to resolve each mode. The highest frequency resolution in a commercially available spectrometer is about 4 GHz in an optical frequency, then the higher repetition rate than 4 GHz is crucial to resolve comb teeth.

Here we report on our recent progress of high-repetition-rate ML oscillator [1]. We are concentrating on the laser-diode (LD) pumped Kerr-lens ML oscillator. There are some reasons to study this type of lasers. Typical high-repetition-rate comb is made by using Ti:sapphire laser pumped by a large green laser which is not easy to keep running for many days. However, many applications of the frequency comb require long-term operation. A single-mode-fiber (SMF) coupled LD can be kept running as long as we need without any degradation or miss alignment. The main drawback is its poor power. The highest power of the SMF coupled LD is limited below 1 W. Lower power pumping makes it difficult to realize high-repetition-rate ML oscillator. We invented new scheme of the ML oscillator with high finesse. This makes the intra-cavity power high enough to realize the Kerr-lens ML. By adopting Yb-doped ceramic as a gain medium, we have realized 6-GHz repetition rate oscillator with femto-second pulse duration.

Figure 1 shows the schematic of the small oscillator. ML oscillator consists of two concave mirrors and two plane mirrors. One of the plane mirror is specially coated

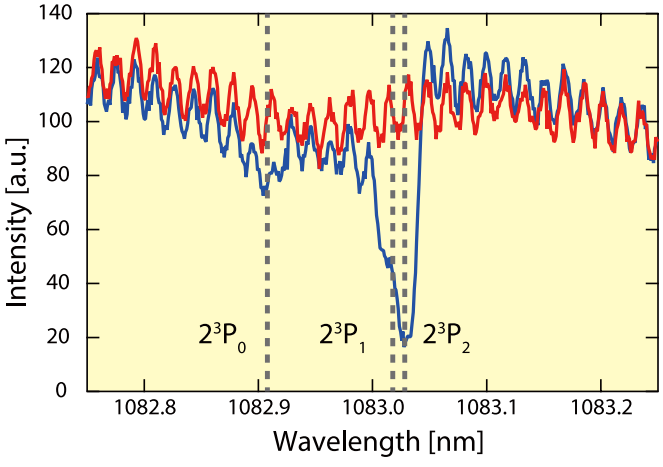

Fig. 2. Absorption spectroscopy of meta-stable He. Red curve shows the laser spectrum without He atoms. The modulation correspond comb structure. Blue curve was obtained with meta-stable He atoms. We can see clear two absorptions that correspond to the triplet S to triplet P transitions in a meta-stable state. 1S-2S transition is strictly prohibited so that the metastable life time is long enough to observe these transitions.

to compensate a chirp in the cavity. 1-mm-thick Yb:Lu_2O_3 ceramic was used for the laser gain. Obtained spectrum width was about 8 nm, and the measured pulse duration was 160 fs. By using commercially available optical spectrum analyzer, each comb mode was clearly resolved. This comb is applied for the precision spectroscopy of meta-stable He atoms, which has three absorption lines in the spectrum of this laser. Figure 2 shows the absorption spectroscopy of He obtained with 5.2-GHz repetition rate at this time. Three lines correspond 2^3S_1- 2^3P_0, 2^3S_1- 2^3P_1 and 2^3S_1- 2^3P_2 transitions. The energy spacing of 2^3P_0- 2^3P_1 is 30 GHz, and that of 2^3P_1- 2^3P_2 is 2 GHz, which is too small to resolve in this setup. The absolute frequency could be determined if the offset frequency is controlled, although it is not realized yet.

We have demonstrated the multi-GHz repetition-rate Kerr-lens ML oscillator with LD pumping for the first time to our best knowledge. It would open new applications with mode-resolved spectroscopy. The astronomical application is one of the promising candidate, in which this kind of laser could be used in order to find extra-solar planets.

Reference

[1] M. Endo, A. Ozawa, and Y. Kobayashi, Opt. Lett. **38**, 4502 (2013).

Authors
M. Endo and Y. Kobayashi

Generation of Attosecond Soft-X-Ray Bursts in the Water Window

Itatani Group

High harmonic generation using intense laser pulses is the most promising method to produce attosecond optical pulses. In the past decade, attosecond science has been extensively exploited using the advanced Ti:sapphire laser technology that can produce attosecond pulses in the extreme ultraviolet (EUV) below 200 eV in photon energies. Recent development of intense infrared sources that are based on optical parametric chirped-pulse amplification (OPCPA) has opened the opportunities to extend the spectral range of high harmonics from the EUV to the soft X ray region, but the lack of well-controlled reliable IR sources has been the problem to realize attosecond soft-X-ray spectroscopy.

In the present research [1], we have developed a novel IR light source that is based on OPCPA using BiB_3O_6 crystals pumped by Ti:sapphire lasers. This OPCPA system can amplify an octave-spanned bandwidth from 1100 to 2200 nm, which enables the phase-stable direct amplification of sub-two-cycle IR pulses. The light source produces 0.5-mJ,

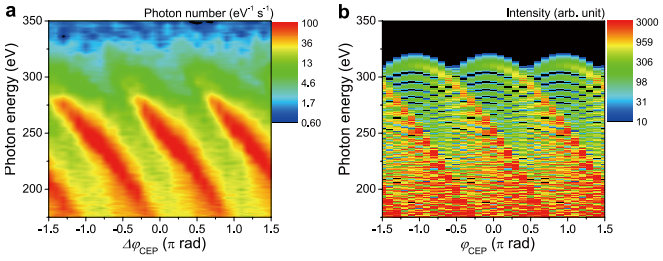

Fig. 1. (a) Experimentally obtained high harmonic spectra recorded at relative carrier-envelope phases in steps of 0.1π rad. (b) Simulated high harmonic spectra assuming 10-fs optical pulses at 1600 nm with an intensity of 4×10^{14} W/cm^2.

9-fs pulses with stable carrier-envelope phases (CEPs) at 1-kHz repetition rate. We have achieved excellent stabilities in the output energy and CEP, which are comparable to those of commercial Ti:sapphire lasers.

Figure 1(a) shows observed high harmonic spectra around the cutoff photon energy as a function of the CEP. The maximum photon energy reaches ~330 eV that is well beyond the carbon *K* edge at 284 eV. The shifting structures of the spectral peak is called the half-cycle cutoff, which is a clear signature of the generation of single isolated attosecond pulses. Figure 1(b) shows simulated results that are based on the strong-field approximation assuming the experimental parameters described in the caption of Fig. 1(a). The good agreement between the experimental and simulation results suggests the generation of isolated attosecond bursts in the water window. This result is an important milestone to extend the attosecond spectroscopy into the soft X ray region where element-specific ultrafast spectroscopy as well as novel attosecond techniques using high-energy electron wavepackets can be explored in the future.

Reference

[1] N. Ishii, K. Kaneshima, K. Kitano, T. Kanai, S. Watanabe, and J. Itatani, Nature Comm. **5**, 3331 (2014).

Authors

N. Ishii, K. Kaneshima, K. Kitano, T. Kanai, S. Watanabe[a], and J. Itatani

[a]Tokyo University of Science